Generalizing Normal Mode Expansion of Electromagnetic Green's Tensor to Open Systems

Parry Y. Chen,[1,2,*] David J. Bergman,[2] and Yonatan Sivan[1]

[1] *Unit of Electro-optic Engineering, Ben-Gurion University, Beersheba, Israel*

[2] *School of Physics and Astronomy, Raymond and Beverly Sackler Faculty of Exact Sciences, Tel Aviv University, Tel Aviv, Israel*

(Received 30 October 2017; revised manuscript received 6 August 2018; published 5 April 2019)

We generalize normal mode expansion of Green's tensor $\bar{\bar{G}}(\boldsymbol{r},\boldsymbol{r}')$ to resonators in open systems, resolving a long-standing open challenge. We obtain a simple yet robust formulation whereby radiation of energy to infinity is captured by a complete, discrete set of modes rather than a continuum. This enables rapid simulations by providing the spatial variation of $\bar{\bar{G}}(\boldsymbol{r},\boldsymbol{r}')$ over both $\boldsymbol{r}$ and $\boldsymbol{r}'$ in one simulation. Systems with or without material losses can be treated. Few eigenmodes are often necessary for nanostructures, facilitating both analytic calculations and unified insight into computationally intensive phenomena such as Purcell enhancement, radiative heat transfer, van der Waals forces, and Förster resonance energy transfer. We bypass all implementation and completeness issues associated with the alternative quasinormal eigenmode methods by defining modes with permittivity rather than frequency as the eigenvalue. We obtain true stationary modes that decay rather than diverge at infinity, and are trivially normalized. Completeness is achieved both for sources located within the inclusion and the background through use of the Lippmann-Schwinger equation. Modes are defined by a linear eigenvalue problem, readily implemented with any numerical method. We demonstrate its simple implementation with COMSOL MULTIPHYSICS using the default inbuilt tools. The results are validated against direct scattering simulations, including analytic Mie theory, attaining arbitrarily accurate agreement regardless of source location or detuning from resonance.

DOI: 10.1103/PhysRevApplied.11.044018

I. INTRODUCTION

Green's functions $G(\boldsymbol{r},\boldsymbol{r}')$ and Green's tensors $\bar{\bar{G}}(\boldsymbol{r},\boldsymbol{r}')$ are essential tools for solving linear wave equations with source terms, being the fundamental solution of a unit impulse. Closed-form expressions of $\bar{\bar{G}}(\boldsymbol{r},\boldsymbol{r}')$ are known for free space and a limited number of simple geometries, but in a general geometry such as an arbitrarily shaped cavity, it has a nontrivial variation over $\boldsymbol{r}$ and $\boldsymbol{r}'$ [1–3]. Numerical simulation is often the only available option, but the computational burden becomes prohibitive if repeated simulations are required for every source position and orientation.

A more palatable alternative is to expand $\bar{\bar{G}}(\boldsymbol{r},\boldsymbol{r}')$ in the basis of the cavity's eigenmodes, which can be obtained from a single simulation. These provide the full spatial variation of $\bar{\bar{G}}(\boldsymbol{r},\boldsymbol{r}')$ over $\boldsymbol{r}$ and $\boldsymbol{r}'$, especially since only a few eigenmodes are often necessary for expansion. Modal expansion of $\bar{\bar{G}}(\boldsymbol{r},\boldsymbol{r}')$ has a long history for conservative systems, such as closed cavities without loss [1]. Here the eigenmodes are *normal modes*, which are stationary states with real eigenfrequencies. These provide a complete and orthogonal basis, with completeness being necessary for a valid expansion of $\bar{\bar{G}}(\boldsymbol{r},\boldsymbol{r}')$. Less straightforward is modal expansion for open systems, a topical problem on which research has intensified recently. Conceptually, the simplest generalization of modal expansion to handle radiation losses is to permit the modes to have complex eigenfrequencies, yielding *quasinormal modes* [4–10]. However, use of quasinormal modes has a number of unwelcome side effects.

We adopt a different approach in this paper. We seek a direct generalization of normal modes to open systems, thus expanding $\bar{\bar{G}}(\boldsymbol{r},\boldsymbol{r}')$ in true stationary states, yielding a result valid for real frequencies, thus solving a problem open since the inception of normal mode expansions. The formulation is applicable without modification to both lossless resonators and resonators with intrinsic material losses. We demonstrate that a generalized normal mode expansion (GENOME) recovers both the simplicity and the rigor of normal modes observed in conservative systems. We specifically treat the electromagnetic Green's tensor, but also remark that GENOME can be applied to any other wave equation, such as for acoustics,

*parryyu@post.bgu.ac.il

elasticity [11,12], quantum mechanical scattering [13], and linearized gravitational waves [14,15].

The electromagnetic Green's tensor $\bar{\bar{G}}(\boldsymbol{r},\boldsymbol{r}')$ is fundamental to the photonic density of states, relating both to the power radiated by a classical dipole antenna and to the spontaneous emission rate of quantum emitters under a semiclassical treatment [3,16]. Green's tensor can be strongly influenced by appropriately designed nanostructures. A broad range of electromagnetic processes and quantum-optics phenomena may be enhanced or altered, including emission from individual atoms and molecules, known as the *Purcell effect*, charge transfer between molecules, known as *Förster resonance energy transfer*, and emission from bulk sources, such as in nonlinear wave mixing, radiative heat transfer, van der Waals forces, quantum friction, super-radiance [17], and strong coupling [18], among others. All such phenomena are linked to $\bar{\bar{G}}(\boldsymbol{r},\boldsymbol{r}')$, owing to its fundamental definition,

$$\nabla \times (\nabla \times \bar{\bar{G}}) - k^2 \epsilon(\boldsymbol{r}) \bar{\bar{G}} = \bar{\bar{I}} \delta^3(\boldsymbol{r} - \boldsymbol{r}'), \tag{1}$$

which gives the electrodynamic response of a detector at $\boldsymbol{r}$ due to a point source at $\boldsymbol{r}'$ radiating at frequency $\omega = ck$ in the presence of a scatterer defined by $\epsilon(\boldsymbol{r})$, where $\bar{\bar{I}}$ is the unit tensor.

To place GENOME in context, we provide a brief review of modal expansions. $\bar{\bar{G}}(\boldsymbol{r},\boldsymbol{r}')$ can be obtained via numerical simulation by placing a radiating dipole at $\boldsymbol{r}'$. Finding the full spatial variation becomes a laborious task, since the location and orientation of the source dipole must be continuously varied, requiring repeated simulation. Instead, modal expansion provides

$$\bar{\bar{G}}(\boldsymbol{r},\boldsymbol{r}') = c^2 \sum_m \frac{\boldsymbol{E}_m(\boldsymbol{r}) \otimes \boldsymbol{E}_m^*(\boldsymbol{r}')}{\omega_m^2 - \omega^2} \tag{2}$$

for conservative systems [1–3,16]. Here ω_m are the eigenfrequencies of each mode, and $\otimes$ defines the outer product between two vectors. Thus, the fields produced by any point source is immediately available by simply evaluating the complex conjugate modal field $\boldsymbol{E}_m^*(\boldsymbol{r}')$ at $\boldsymbol{r}'$. The same eigenmode $\boldsymbol{E}_m(\boldsymbol{r})$ also gives variation over detector positions $\boldsymbol{r}$, thus providing unified analytic insight across a wide variety of optical phenomena. Indeed, often a single mode suffices, since the detuning $\omega_m^2 - \omega^2$ from the other resonances is typically large when the nanostructure is small. All nine tensor components are available, which would otherwise require nine separate simulations for each $\boldsymbol{r}'$ [19]. Finally, the total fields $\boldsymbol{E}(\boldsymbol{r})$ produced by bulk sources, or any arbitrary source distribution $\boldsymbol{J}(\boldsymbol{r}')$, can be calculated with the same ease: by superposing contributions from different source positions,

$$\boldsymbol{E}(\boldsymbol{r}) = i\omega\mu_0 \int \bar{\bar{G}}(\boldsymbol{r},\boldsymbol{r}') \cdot \boldsymbol{J}(\boldsymbol{r}') dV', \tag{3}$$

where $\bar{\bar{G}}(\boldsymbol{r},\boldsymbol{r}')$ is expanded using Eq. (2), yielding overlap integrals between $\boldsymbol{J}(\boldsymbol{r}')$ and $\boldsymbol{E}_m^*(\boldsymbol{r}')$.

The expansion (2) is adequate when losses are negligible. However, resonators with non-negligible losses have attracted significant research attention recently, particularly plasmonic nanoresonators, consisting, for example, of a metallic inclusion in a uniform background. Metal-dielectric interfaces produce sharp field concentrations, generating electromagnetic hot spots ideal for influencing the density of states. However, energy is lost due to material absorption, and is continuously radiated into the background. These losses can be treated in a modal expansion by coupling to the material degrees of freedom [20], and the continuum of background electromagnetic modes [21], respectively. But the utility of Eq. (2) is diminished since the expansion ceases to be via a limited set of discrete electromagnetic modes.

Expansion via a discrete set is once again possible with quasinormal modes, yielding an expression similar to Eq. (2) [9,22–25]. Discreteness stems from imposing Sommerfeld radiation boundary conditions to account for radiation [26]. The imaginary part of the complex eigenfrequency relates to the finite lifetime or decay rate of energy to all loss channels. However, complex eigenfrequencies introduce their own implementational and interpretational difficulties, such as a difficult to solve nonlinear eigenvalue problem, the need to define permittivities at complex frequencies, and exponentially diverging fields, which are unphysical at real frequencies. More fundamentally, quasinormal modes provide only a complete expansion for source positions $\boldsymbol{r}'$ inside the resonator [25,27], giving inaccuracies for exterior sources. Nevertheless, quasinormal modes yield very satisfactory results for many practical applications, as much progress has been achieved in the past several years in their development and in overcoming their previous limitations. See Sec. III for further details.

GENOME bypasses these complexities, providing many advantages, both fundamental and practical. Instead of using complex frequency modes to account for loss, true stationary modes are obtained by designating the permittivity of the nanostructure ϵ_m to be the complex eigenvalue. Thus, we fix a real k, and also fix the inclusion's geometry and background permittivity of the simulation domain, consequently determining the complex ϵ_m that brings the system to resonance. Our GENOME approach is based on the *spectral decomposition* formalism first developed in a series of papers by Bergman and coworkers for electrostatics [28,29] and then electrodynamics [30,31], with similar methods having been developed independently by

others [32–35]. In the electrostatic limit, the formalism has been used for applications such as spasers [36], self-similar antennas [37], disordered media [38,39], and second-harmonic generation [40,41], as well as for the computation of effective medium parameters, bounds on them, and associated sum rules [29,37,42]. In the electrodynamic limit, it has been used for spherical and Veselago-Pendry lens geometries [30,31], and for the analysis of lifetime calculations [43] and second-harmonic generation, in particular, resolving long-standing ambiguities on the definitions of boundary conditions for surface second-harmonic generation [44].

Completeness is an important consideration, being necessary for successful modal expansion [1]. Direct expansion using eigenmodes, including our eigenpermittivity modes, is insufficient to give completeness everywhere. Key to the success of GENOME is use of the Lippmann-Schwinger equation, which extends completeness from interior sources to all exterior sources $\boldsymbol{r}'$ and all detector locations $\boldsymbol{r}$ [30]. Use of the Lippmann-Schwinger equation distinguishes GENOME from other methods that also use eigenpermittivity modes, such as constant flux states [45]. Thus, GENOME converges to the correct solution with arbitrary precision as more eigenmodes are considered, regardless of detuning from the inclusion's resonances and source or detector coordinates. Unlike Eq. (2), our expansion also efficiently reproduces the divergence and nontransverse components of $\bar{\bar{G}}(\boldsymbol{r},\boldsymbol{r}')$ at the source, without requiring many modes.

Modal completeness affords great practical utility. Crucially, modes of analytically insoluble systems can be generated effortlessly and reliably using the modes of a simpler system as a basis. For example, since quasinormal modes are complete internally, modes of a sphere can generate modes of wedges or any arbitrary shape enclosed by the sphere [46], such as split-ring resonators. A compelling benefit of GENOME over quasinormal modes is that the modes of clusters and arrays of nanostructures can be obtained from known modes of the constituents without further numerical simulation, for example, obtaining dimer modes from monomer modes [29,30]. This constitutes a generalization of the celebrated theory of linear combination of molecular orbitals to electromagnetic structures [47,48], and provides a rigorous generalization of an approximate hybridization approach developed in the context of nanoplasmonics [49].

Our generalized normal modes remain well behaved throughout all space, since frequency and background permittivity remain real and physical. In particular, our eigenmodes both decay to zero at infinity and satisfy the vector equivalent of the Sommerfeld radiation condition, the Silver-Müller condition. In contrast to quasinormal modes, this corresponds to the physical far-field solution and yields the correct energy radiated into the background. Consequently, normalization of modes is also rapid and trivial, achieved by a volume integral over the inclusion's interior.

Our modes are always generated by a linear eigenvalue equation, even when material dispersion is present. Thus, eigenmode search is simple and readily automated, with no need for delicate root searches in the complex plane, instead relying on the many powerful, robust linear-algebra algorithms. We demonstrate its straightforward general implementation in COMSOL MULTIPHYSICS, a commercially available finite-element package, by adapting its inbuilt eigenfrequency solver with a simple substitution trick. Due to the simplicity of the linear eigenvalue equation, implementation via any method capable of producing eigenmodes is possible, including volume-integral methods, the discrete-dipole approximation, and plane-wave expansion. Analytic solutions are also available for simple spherical, cylindrical, and planar geometries [30,31,50].

The paper is organized as follows. In Sec. II, we develop GENOME for lossy, open systems. The exposition is relatively self-contained, but technical proofs are omitted, focusing instead on conveying underlying insight into the properties of our method. Special attention is given to the generalized normal modes in Sec. II B. In Sec. III, we offer a comprehensive comparison between GENOME and the alternative quasinormal mode expansion. Section IV details the brief numerical implementation in COMSOL MULTIPHYSICS, with numerical examples that demonstrate the completeness of GENOME. Further discussion on the properties of eigenpermittivity modes is also provided. Section V presents a summary and conclusion.

II. GENERALIZED NORMAL MODE EXPANSION

A. Lippmann-Schwinger equation

The foundation of GENOME is the Lippmann-Schwinger equation for electrodynamics, which is also the basis of two families of related numerical schemes: method of moments (MoM) and discrete dipole approximation (DDA), also known as volume-integral or coupled-dipole methods, respectively [3,51–53]. In quantum mechanics, the Lippmann-Schwinger equation is used for scattering calculations, and is commonly solved using the Born approximation or Born series.

The Lippmann-Schwinger equation is obtained from Maxwell's equations,

$$\nabla \times (\nabla \times \boldsymbol{E}) - k^2 \epsilon(\boldsymbol{r}) \boldsymbol{E} = i\omega\mu_0 \boldsymbol{J}, \tag{4}$$

assuming harmonic $e^{-i\omega t}$ time variation and nonmagnetic media. We begin by assuming that the structure defined by its permittivity profile $\epsilon(\boldsymbol{r})$ rests in a background of uniform permittivity ϵ_b. This permits the manipulation of Eq.

(4) to yield

$$\nabla \times (\nabla \times \boldsymbol{E}) - k^2 \epsilon_b \boldsymbol{E} = i\omega\mu_0 \boldsymbol{J} + k^2(\epsilon(\boldsymbol{r}) - \epsilon_b)\boldsymbol{E}. \quad (5)$$

In Eq. (4), notice that $\boldsymbol{J}$, the imposed free-current source, sits alone on the right hand side, while the response of the inclusion is on the left hand side. In Eq. (5), both $\boldsymbol{J}$ and the response of the inclusion are on the right hand side, and the second term can be interpreted as the bound currents produced by the inclusion.

Since the operator on the left hand side of Eq. (5) is no longer a function of $\boldsymbol{r}$, Eq. (5) can be solved using the simple Green's function for uniform media,

$$\nabla \times (\nabla \times \bar{\bar{G}}_0) - k^2 \epsilon_b \bar{\bar{G}}_0 = \bar{\bar{I}}\delta^3(\boldsymbol{r} - \boldsymbol{r}'), \quad (6)$$

which has a simple known analytic form $\bar{\bar{G}}_0(|\boldsymbol{r} - \boldsymbol{r}'|)$ depending on the dimensionality of the problem [2]. Application of Eq. (6) to both terms on the right hand side of Eq.(5) yields its Green's function solution, which is the desired Lippmann-Schwinger equation:

$$\boldsymbol{E}(\boldsymbol{r}) = \boldsymbol{E}_0(\boldsymbol{r}) + k^2 \int \bar{\bar{G}}_0(|\boldsymbol{r} - \boldsymbol{r}'|)(\epsilon(\boldsymbol{r}') - \epsilon_b)\boldsymbol{E}(\boldsymbol{r}')d\boldsymbol{r}'. \quad (7)$$

The term $\boldsymbol{E}_0(\boldsymbol{r})$ is the known radiation pattern of external sources in a uniform background,

$$\boldsymbol{E}_0(\boldsymbol{r}) = i\omega\mu_0 \int \bar{\bar{G}}_0(|\boldsymbol{r} - \boldsymbol{r}'|)\boldsymbol{J}(\boldsymbol{r}')d\boldsymbol{r}', \quad (8)$$

which is simple to solve since it is independent of the inclusion. In particular, standard textbook expressions are available for the $\boldsymbol{E}_0(\boldsymbol{r})$ of point dipoles and other simple source configurations [54].

Crucial to the Lippmann-Schwinger equation is that the same simple Green's tensor appears in both Eq. (7) and Eq. (8), a property exploited by all resultant methods, including GENOME. As mentioned, the Lippmann-Schwinger equation (7) can be solved numerically. This involves spatial discretization, recasting Eq. (7) in linear-algebra form, which sometimes requires iterative solution until convergence [55]. This is due to the implicit nature of Eq. (7), with the desired solution $\boldsymbol{E}(\boldsymbol{r})$ appearing inside the integral, thus forming a Fredholm integral equation of the second kind. The Lippmann-Schwinger equation can also be expanded in terms of basis functions, such as the cylindrical harmonic functions, again yielding a linear-algebra problem, but obviating the need for iterative solution [56].

We use the Lippmann-Schwinger equation as the foundation of a yet more powerful analytic method. Instead of solving Eq. (7) directly, we first find its stationary or self-sustaining solutions, corresponding exactly to the eigenpermittivity modes of the inclusion. By projecting onto this basis, we obtain an analytic solution of the Lippmann-Schwinger equation (7). We then obtain the desired eigenmode expansion of Eq. (1), which, unlike Eq. (6), may be regarded as the *dressed Green's tensor*. The solution is rigorous and valid everywhere even though the eigenmodes form a complete set only in the interior. This follows from a key property of the Lippmann-Schwinger equation, enabling $\boldsymbol{E}(\boldsymbol{r})$ to be determined everywhere from knowledge of $\boldsymbol{E}(\boldsymbol{r})$ inside the inclusion only, where $\epsilon(\boldsymbol{r}) - \epsilon_b$ is nonzero.

B. The generalized normal modes

To proceed with GENOME, we define the appropriate normal modes of the system. We also outline some key properties, from which many of the advantages of the method stem. The eigenvalue equation is obtained by neglecting $\boldsymbol{E}_0$ in Eq. (7). At this point, we simplify the formulation by assuming that the permittivity of the inclusion is uniform so that the simulation domain is defined by only two permittivities: an eigenpermittivity ϵ_m applicable to the inclusion's interior, and the fixed background ϵ_b. This yields the simplified eigenvalue equation

$$s_m \boldsymbol{E}_m(\boldsymbol{r}) = -\epsilon_b k^2 \int \bar{\bar{G}}_0(|\boldsymbol{r} - \boldsymbol{r}'|; k^2)\theta(\boldsymbol{r}')\boldsymbol{E}_m(\boldsymbol{r}')d\boldsymbol{r}', \quad (9)$$

where s_m is the mth eigenvalue, known as the *Bergman spectral parameter* [57],

$$s_m \equiv \frac{\epsilon_b}{\epsilon_b - \epsilon_m}, \quad (10)$$

$\theta(\boldsymbol{r})$ is a step function that is unity inside the inclusion and zero elsewhere, and the dependence of the Green's tensor on k^2 is explicitly noted. The eigenvalue (10) is defined to conform to previous definitions (c.f. Bergman and Stroud [30]), though some differences in Eq. (9) remain, stemming from differing definitions of the free-space Green's tensor (6).

The eigenvalue in Eqs. (9) and (10) is ϵ_m, representing the inclusion permittivity, which contrasts with the more prevalent choice, k. In other words, k is held fixed, while ϵ_m is varied until the inclusion is at resonance. As a simple example, the modes of a sphere can be determined by the poles of its scattering matrix, which for quasistatic fields varies as $(\epsilon_i - \epsilon_b)/(\epsilon_i + 2\epsilon_b)$ [58]. Thus, the eigenpermittivity at long wavelengths is $\epsilon_m = -2\epsilon_b$. By specifying k to be real, we obtain stationary modes. Moreover, the free-space Green's tensor decays appropriately rather than diverging as $\boldsymbol{r} \to \infty$, as do the resulting eigenmodes. This choice also leads to a linear eigenvalue problem, since $\bar{\bar{G}}_0(|\boldsymbol{r} - \boldsymbol{r}'|; k^2)$ is not a function of ϵ_m.

The modes, in general, have complex eigenvalues ϵ_m, with the imaginary part corresponding to gain across the interior of the inclusion. This gain compensates for the

energy lost from the inclusion due to radiation, permitting the mode to remain in a stationary state. Thus, the complex eigenpermittivity has a simple interpretation, being the lasing threshold of the inclusion at a particular frequency [45,57]. Despite the similarity between Eq. (7) and Eq. (9), the eigenvalues ϵ_m are, in general, unrelated to the actual permittivity of the inclusion to be solved in Eq. (7). The actual permittivity is specified later in Eq. (21), with the modes $\boldsymbol{E}_m$ serving as a complete orthonormal mathematical basis [30]. The only information from Eq. (7) that remains in Eq. (9) is the frequency, and the geometry of the inclusion captured by $\theta(\boldsymbol{r})$. In that sense, our formulation separates the material properties from geometric properties, so the imaginary part of ϵ_m needs to account for only radiation losses experienced by the geometry. Indeed, the magnitude of $\mathrm{Im}(\epsilon_m)$ can be used to quickly identify whether a mode is bright or dark. Furthermore, the eigenmodes are applicable to any uniform inclusion permittivity, even complex permittivities, without modification.

In passing, we mention that the restriction to inclusions with a uniform isotropic permittivity in Eq. (9) is not necessary. Generalizations to nonuniform and anisotropic inclusions are possible. The eigenmodes would still be defined by Eq. (9), but $\theta(\boldsymbol{r})$ would no longer be a step function, requiring generalization to reflect the $\bar{\bar{\epsilon}}(\boldsymbol{r})$ profile to be simulated. The eigenvalues are still s_m, but their interpretation as the eigenpermittivities of the inclusion (10) would no longer be valid. Lastly, nonuniform or anisotropic background media are possible, by using the relevant Green's tensor in place of $G_0(|\boldsymbol{r}-\boldsymbol{r}'|)$ [59,60].

C. Expansion via normal modes

We take as given that the relatively simple task of finding the radiation pattern in the uniform background $\boldsymbol{E}_0$ in Eq. (8) is complete. The final stage of GENOME is to solve the Lippmann-Schwinger equation (7) by using its normal modes, Eq. (9), to expand the source $\boldsymbol{J}(\boldsymbol{r})$. We largely follow the derivation in Ref. [30]. For notational brevity, we begin by casting the Lippmann-Schwinger equation (7) in operator form:

$$\boldsymbol{E} = \boldsymbol{E}_0 + u\hat{\Gamma}\hat{\theta}\boldsymbol{E}, \tag{11}$$

where u now describes the permittivity of the actual inclusion ϵ_i,

$$u \equiv \frac{\epsilon_b - \epsilon_i}{\epsilon_b}. \tag{12}$$

$\hat{\Gamma}$ is an integral operator incorporating the Green's function along with k, and $\hat{\theta}$ is the operator form of $\theta(\boldsymbol{r})$, which zeros the field outside the inclusion, so

$$\hat{\Gamma}\hat{\theta}\boldsymbol{E} \equiv -\epsilon_b k^2 \int \bar{\bar{G}}_0(|\boldsymbol{r}-\boldsymbol{r}'|)\theta(\boldsymbol{r}')\boldsymbol{E}(\boldsymbol{r}')d\boldsymbol{r}'. \tag{13}$$

The formal solution to Eq. (11) is

$$\boldsymbol{E} = \frac{1}{1-u\hat{\Gamma}\hat{\theta}}\boldsymbol{E}_0. \tag{14}$$

In spectral theory, the operator $(1-u\hat{\Gamma}\hat{\theta})^{-1}$ in Eq. (14) is known as the *resolvent* [61]. Our solution for the unknown field $\boldsymbol{E}$ proceeds by projecting the known $\boldsymbol{E}_0$ onto the known normal modes $\boldsymbol{E}_m$. Specifically, we define the projection operator $\hat{I}$, which in bra-ket notation is

$$\hat{I} = \sum_m \hat{\theta}|E_m\rangle\langle E_m|\hat{\theta}. \tag{15}$$

This simple form is valid because the modes obey a biorthogonality relation [30]. By including $\hat{\theta}$ in $\hat{I}$, we expand only over the interior fields. This avoids an unwieldy integral over all space, and also expands only in the region where the eigenmodes provide a complete basis. This projection operator assumes that the modes are normalized,

$$\langle E_m|\hat{\theta}|E_m\rangle = 1. \tag{16}$$

To ensure that the units are correct, it is convenient to define the bra and the ket to have inverse units with respect to each other. The unknown field $|E\rangle$ is then

$$\hat{\theta}|E\rangle = \sum_m \hat{\theta}|E_m\rangle\langle E_m|\frac{\hat{\theta}}{1-u\hat{\Gamma}\hat{\theta}}|E_0\rangle. \tag{17}$$

Next is the key step of GENOME. Instead of applying the operator $(1-u\hat{\Gamma}\hat{\theta})^{-1}$ to $|E_0\rangle$, which would result in a lengthy numerical calculation via the Born series, we exploit the freedom offered by the unified nature of the Green's function in Eqs. (8) and (9) to operate on $\langle E_m|$ instead, immediately yielding an exact analytic solution. We invoke the adjoint form of eigenvalue equation (9):

$$\langle E_m|\hat{\theta}\hat{\Gamma} = \langle E_m|s_m. \tag{18}$$

It is critical here that the eigenmodes (9) share a predefined frequency equivalent to the desired k of the Lippmann-Schwinger equation (7) to be solved. This enables the aforementioned freedom to interchange, since the Green's tensors represented by $\hat{\Gamma}$ in Eqs. (17) and (18) are identical. This obtains from Eq. (17) the total interior field $\hat{\theta}|E\rangle$,

$$\hat{\theta}|E\rangle = \sum_m \hat{\theta}|E_m\rangle\frac{1}{1-us_m}\langle E_m|\hat{\theta}|E_0\rangle, \tag{19}$$

expressed in terms of overlap integrals.

To obtain the fields everywhere, Eq. (19) is inserted into the original Lippmann-Schwinger equation (11), this time

operating $\hat{\Gamma}\hat{\theta}$ on $|E_m\rangle$ to give

$$|E\rangle = |E_0\rangle + \sum_m |E_m\rangle \frac{us_m}{1-us_m}\langle E_m|\hat{\theta}|E_0\rangle. \quad (20)$$

Thus, with the aid of the Lippmann-Schwinger equation, we have obtained an expansion valid over all space even though we expanded the fields only inside the inclusion. For convenience, Eq. (20) can be expressed explicitly in terms of permittivities:

$$|E\rangle = |E_0\rangle + \sum_m |E_m\rangle \frac{\epsilon_i-\epsilon_b}{\epsilon_m-\epsilon_i}\langle E_m|\hat{\theta}|E_0\rangle. \quad (21)$$

Equation (21) expresses the total fields of the system in terms of the radiation of the source in a uniform medium, with additional contributions from modes of the inclusion that are excited. The weight of each eigenmode is determined in part by the detuning between the inclusion permittivity, ϵ_i, and the eigenmode, ϵ_m. The eigenmode with the most similar permittivity is the dominant contributor to the radiated energy, and the series converges rapidly toward the true solution. Secondly, the electrodynamic interaction between the source and the inclusion is entirely encoded within the geometric factor $\langle E_m|\hat{\theta}|E_0\rangle$, representing the spatial overlap between the incident field and the mode being excited. The explicit form of this overlap integral is presented in Appendix A. The solution (21) is exact up to truncation in m, since the Born series is avoided in obtaining Eq. (19), and arbitrary accuracy is possible by increasing m. The one set of eigenmodes $|E_m\rangle$ is applicable to all possible inclusion permittivities ϵ_i and excitations $|E_0\rangle$, the latter requiring only the evaluation of the overlap integral, which represents a small fraction of the total simulation time.

The solution (21) is the most suitable form when the source is in the far field, so $|E_0\rangle$ has a known form, such as a plane wave or a beam. If, however, the source is in the near field, a second formulation is more convenient, expressed directly in terms of sources $\boldsymbol{J}(\boldsymbol{r})$ [31]. This begins by casting Eq. (8) into operator form, yielding

$$|E_0\rangle = -\frac{i}{\omega\epsilon_0\epsilon_b}\hat{\Gamma}|J\rangle. \quad (22)$$

After inserting Eq. (22) into Eq. (20), we obtain

$$|E\rangle = |E_0\rangle - \frac{i}{\omega\epsilon_0\epsilon_b}\sum_m |E_m\rangle \frac{us_m}{1-us_m}\langle E_m|\hat{\theta}\hat{\Gamma}|J\rangle. \quad (23)$$

Again, by applying the operator $\hat{\theta}\hat{\Gamma}$ to $\langle E_m|$ via Eq. (18) rather than $|J\rangle$, we obtain a simple solution:

$$|E\rangle = |E_0\rangle - \frac{i}{\omega\epsilon_0\epsilon_b}\sum_m |E_m\rangle \frac{us_m^2}{1-us_m}\langle E_m|J\rangle. \quad (24)$$

In terms of permittivities, Eq. (24) can be rewritten as

$$|E\rangle = |E_0\rangle + \frac{i}{\omega\epsilon_0}\sum_m |E_m\rangle \frac{\epsilon_i-\epsilon_b}{(\epsilon_m-\epsilon_i)(\epsilon_m-\epsilon_b)}\langle E_m|J\rangle, \quad (25)$$

yielding an expression of the form (3). The resulting equation (25) is largely similar to Eq. (21), but the integral $\langle E_m|J\rangle$ is now no longer restricted to the interior of the inclusion, and receives contributions from all locations where $\boldsymbol{J}(\boldsymbol{r})$ is nonzero. Nevertheless, Eq. (25) remains a rigorous solution of the Lippmann-Schwinger equation and still benefits from the completeness of the eigenmodes within the interior.

Finally, the desired normal mode expansion of Green's tensor (1), applicable to resonators in open and lossy systems, is obtained by choosing $\boldsymbol{J}(\boldsymbol{r})$ to be a localized Dirac-δ source. By the sifting property of Dirac-δ functions, the weight factor $\langle E_m|J\rangle$ is simply the amplitude of the adjoint mode at the source location, $\boldsymbol{E}_m^\dagger(\boldsymbol{r})$. The Green's tensor is then constructed from its three components, giving

$$\bar{\bar{G}}(\boldsymbol{r},\boldsymbol{r}') = \bar{\bar{G}}_0(|\boldsymbol{r}-\boldsymbol{r}'|) + \frac{1}{k^2}\sum_m \frac{\epsilon_i-\epsilon_b}{(\epsilon_m-\epsilon_i)(\epsilon_m-\epsilon_b)} \times \boldsymbol{E}_m(\boldsymbol{r})\otimes\boldsymbol{E}_m^\dagger(\boldsymbol{r}'), \quad (26)$$

where $\bar{\bar{G}}_0(|\boldsymbol{r}-\boldsymbol{r}'|)$ is the Green's tensor of the uniform background, Eq. (6). The adjoint field $\boldsymbol{E}_m^\dagger(\boldsymbol{r}')$ is discussed in Appendix A. Compared with Eq. (2), three differences are immediately apparent: the switch from eigenfrequencies to eigenpermittivities, the extra term $\bar{\bar{G}}_0(|\boldsymbol{r}-\boldsymbol{r}'|)$, and the extra factor $(\epsilon_i-\epsilon_b)/(\epsilon_m-\epsilon_b)$. The extra term accounts for the divergence and longitudinal component of $\bar{\bar{G}}(\boldsymbol{r},\boldsymbol{r}')$ at $\boldsymbol{r}'$, while both the extra term and the extra factor ensure the validity of Eq. (26) for all external sources, even though the eigenmodes form a complete basis only in the interior. The extra factor vanishes at resonance, whereby Eq. (26) features the more usual weight $(\epsilon_m-\epsilon_i)^{-1}$. We demonstrate the importance of the extra term and extra factor in Sec. IV. Finally, $\bar{\bar{G}}(\boldsymbol{r},\boldsymbol{r}')$ becomes singular as $\boldsymbol{r}$ approaches $\boldsymbol{r}'$, and is longitudinal at $\boldsymbol{r}=\boldsymbol{r}'$. The term $\bar{\bar{G}}_0$ efficiently captures both aspects, even when expanding in terms of a small set of exclusively transverse modes.

III. COMPARISON WITH QUASINORMAL MODES

Quasinormal mode expansion has recently become a popular and successful generalization of Eq. (2) to lossy resonators in open systems. Alternatively, such modes are known as *resonant states* among other leading proponents [9,46,62,63]. First introduced for quantum mechanical scattering in the context of nuclear physics [4], these

modes were later also introduced for electrodynamics problems [5,6]. Quasinormal modes are defined by the eigenvalue equation

$$\nabla \times (\nabla \times \boldsymbol{E}_m) - \frac{\omega_m^2}{c^2}\epsilon(\boldsymbol{r}, \omega_m)\boldsymbol{E}_m = 0, \tag{27}$$

which yields the Green's tensor expansion [9,22–25]:

$$\bar{\bar{G}}(\boldsymbol{r}, \boldsymbol{r}') = c^2 \sum_m \frac{\boldsymbol{E}_m(\boldsymbol{r}) \otimes \boldsymbol{E}_m(\boldsymbol{r}')}{2\omega_m(\omega_m - \omega)}. \tag{28}$$

A variation of Eq. (28) exists that is equivalent [25], as well as an alternative based on a scattered-field representation [64,65]. The fundamental difference between quasinormal mode expansion and GENOME is the use of complex eigenfrequencies ω_m rather than complex eigenpermittivities ϵ_m to account for loss in lossy and open systems. However, this one change has many ramifications, ranging from the fundamental to the practical. Because of the topical nature of quasinormal mode expansions, we devote this section to a thorough comparison of the advantages and disadvantages of the two methods.

A. Completeness

The completeness of quasinormal modes has been extensively discussed in the literature [21,22,27], being necessary for the validity of Eq. (28). Rigorous proof shows that quasinormal modes form a complete set inside the inclusion, since a sharp interface at the inclusion boundary ensures that fields of sufficiently high spatial frequency are generated within via refraction to represent any field. However, the lack of sharp boundaries enclosing the background means that fields of sufficiently high spatial frequency are not generated [21,27]. Thus, Eq. (28) is rigorously valid only when $\boldsymbol{r}'$ is interior to the inclusion, but not when it is in the background. In contrast, GENOME (26) is complete for sources both inside and outside the inclusion, despite also using modes (9) that are complete only inside the inclusion. Specifically, GENOME contains an extra term and extra factor (26) relative to Eq. (28), which can both be neglected on resonance. Hence, our expansion always converges to arbitrary accuracy regardless of detuning from resonance and the distance from the resonator. We demonstrate this property with numerical examples in Sec. IV.

For many practical applications, the formal lack of completeness of quasinormal modes is not so consequential, especially for Purcell-factor calculations. Quasinormal expansion (28) has been demonstrated to provide excellent numerical agreement even for exterior sources in numerous cases when the response is dominated by a few resonances [10,24,65–67]. It is also claimed that formal issues of completeness may be bypassed in some practical implementations, where infinite space is mapped onto a finite simulation domain, thus finding all necessary modes [68]. This logic can be contrasted with the arguments of Leung *et al.* [27] and Ching *et al.* [21]. Nevertheless, abnormalities can emerge away from resonance, such as negative scattering cross sections [10,64]. Meanwhile, other applications have more-stringent requirements for completeness. For example, it is vital to the success of "perturbation" methods, whereby known modes of simple structures can be used to generate modes of a more-complex structure, a process described in more detail in Sec. IV.

A key advantage of modal expansions that use either quasinormal modes or eigenpermittivity modes is that they treat open systems using only a discrete set of modes, avoiding the cumbersome continuum of radiation modes. Unfortunately, this advantage of quasinormal modes is lost when treating certain geometries, such as two-dimensional (2D) structures or three-dimensional resonators mounted on substrates [9,68,69]. In addition to the usual discrete set of modes, a continuous set of modes now emerges from the eigenvalue equation (27) to account for a branch cut in the underlying dispersion relation. These modes transform the expansion (28) into an expression involving both a sum and an integral. Neglecting the continuum can lead to significant errors, especially for subwavelength resonators. However, when it is included, the continuum requires an additional discretization scheme [9]. In contrast, we have demonstrated in the context of 2D dispersion relations that our eigenpermittivity modes do not experience any branch cuts, and a discrete set emerges from our eigenvalue equation (9) [50].

Lastly, our generalized normal modes are always biorthogonal, and projection and expansion always proceed via Eq. (26), so the relative modal contributions remain obvious from the detuning. Meanwhile, the biorthogonality normally enjoyed by quasinormal modes is disrupted by material dispersion, which requires a more elaborate projection procedure when more than one mode provides a significant contribution [10,24]. This involves evaluating overlap integrals between the modes and then inverting a linear system of equations [10,24]. This issue can be avoided by expansion via the Mittag-Leffler theorem, which shows that Eq. (28) remains true for interior sources even in the presence of dispersive $\epsilon(\boldsymbol{r}, \omega)$ [70,71].

B. Far fields and normalization

A hallmark peculiarity of quasinormal modes is their far-field behavior, diverging exponentially as $\boldsymbol{r} \to \infty$. This is unphysical behavior when treating problems associated with real frequencies, and arises as an unavoidable consequence of complex eigenfrequencies in conjunction with

radiating boundary conditions [7]. Divergence is imperceptible near the resonator, but dominates at further distances, with the divergence becoming noticeable earlier as $\mathrm{Im}(\omega_m)$ increases. Both source and detector coordinates of $\bar{\bar{G}}(\boldsymbol{r},\boldsymbol{r}')$ are affected, producing incorrect Purcell factors and radiation patterns (see, e.g., Ref [65]). A remedy for quasinormal modes exists by numerically generating regularized modes from the original modes, via the Lippmann-Schwinger equation [65]. However, this assumes the response is dominated by a single mode, neglecting all other modes. Meanwhile, our eigenpermittivity modes are valid over the entire domain, both satisfying radiating boundary conditions and decaying to zero as $\boldsymbol{r}\to\infty$. This is the advantage of using eigenmodes of the Lippmann-Schwinger equation itself, defined at real frequencies.

The divergence of quasinormal modes complicates normalization, since any integral over the entire domain correspondingly diverges. Normalization is necessary for projection, so quasinormal modes were previously unsuitable for quantitative studies. More recently, pioneering efforts by several groups have led to several successful normalization schemes. Firstly, the diverging volume integral during normalization can be counterbalanced by a surface integral [7–9,25]. However, some care is required when positioning the surface integral to avoid numerical sensitivity issues [25,72]. See, for example, Ref. [72] and associated comments and replies [73,74] for a detailed discussion. The procedure is also inapplicable for backgrounds with nonuniform permittivity $\epsilon(\boldsymbol{r},\omega)$. Next, divergence can be quelled by perfectly matched layers along the simulation domain boundary, yielding a finite normalization integral [10]. But this method can be inconvenient or even impossible to use unless a perfectly matched layer is used during simulation [72]. For example, resonators coupled to waveguides or periodic boundary conditions require separate treatment [75–77]. Estimates of the normalization constant can also be reverse engineered by comparing the quasinormal mode expansion with a separate simulation using a test source, though this approximation is valid only for individual isolated resonances [64].

In comparison, a simple, general, and robust method exists to normalize our generalized normal modes, achieved by simply integrating the modes over the interior of the inclusion. Indeed, in our COMSOL MULTIPHYSICS implementation, we evaluate the necessary overlap integral of the mode with itself using simply the builtin volume integration tool.

C. Other comparisons

A vital practical consideration is the ease of generating the eigenmodes. Generalized normal modes are always defined by a single linear eigenvalue problem (9), and a rapid robust solution is possible via the many powerful linear-algebra packages. Furthermore, immediate implementation with a range of off-the-shelf simulation packages is possible. Quasinormal modes are relatively more difficult to find numerically since they are defined by a nonlinear eigenvalue problem (27). The nonlinearity originates from the boundary conditions of the open system, since the eigenfrequency explicitly enters the Sommerfeld radiation condition [23]. This can be avoided in many numerical implementation through use of perfectly matched layers. An additional nonlinearity is introduced when material dispersion is present, since frequency appears within $\epsilon(\boldsymbol{r},\omega)$ in Eq. (27). This nonlinearity can also be eliminated. The first method involves perturbing modes of a nondispersive system [71], while the second introduces auxiliary fields [78–80], though this requires additional implementational effort and increases the number of equations to be solved.

To handle the nonlinearity, solutions for quasinormal modes commonly rely on a complex root search, requiring numerical iteration of Eq. (28) until a resonance is located. Accurate initial guesses of the eigenfrequencies are paramount, and it is impossible to guarantee that all relevant solutions have been found. These difficulties can be ameliorated by first analyzing the scattering spectrum of the target nanostructure, obtained through a separate numerical simulation using a broadband source. The real and imaginary parts of ω_m can be estimated from the peaks and linewidths of the spectrum. However, dark modes, low quality-factor modes, and members of closely spaced resonances can remain elusive.

Finally, quasinormal modes require the inclusion permittivity $\epsilon(\boldsymbol{r},\omega)$ to be defined for complex frequencies, which is awkward to measure experimentally. Furthermore, the search for quasinormal modes cannot proceed unless $\epsilon(\boldsymbol{r},\omega)$ is a sufficiently smooth function of frequency. This can preclude use of tabulated or experimentally measured permittivity data. Hence, approximations such as the Drude model are necessary, requiring extension to complex frequencies by analytic continuation.

The preceding discussion and subsections surveyed the advantages of GENOME over quasinormal mode expansion. Currently, quasinormal modes hold one key advantage over generalized normal modes: Eq. (28) is valid for all frequencies [25] so long as all aforementioned provisos are heeded. An approximate analytic expression can also be derived for the line shapes of lossy resonators when a single quasinormal mode is dominant [10,24]. This enables great utility, as line shapes are often the most-accessible quantity in experiments. In contrast, generalized normal modes are defined for an individual frequency. To obtain expansions (26) at other frequencies, a new set of eigenmodes must be generated for each frequency. This represents the sacrifice necessary at present for a rigorous, robust eigenmode expansion of Green's tensor in an open, lossy system.

However, this limitation of generalized normal modes is not fundamental. Firstly, once the eigenmodes have been obtained at one frequency, its eigenpermittivities at neighboring frequencies can be obtained perturbatively. To first order, the eigenmodes are also valid for a range of frequencies [32]. This allows the detuning factor in Eq. (26) to be reexpressed in terms of frequencies [32]. Furthermore, since the eigenmodes are complete, modes defined for one frequency are always able to represent modes at any other frequency via linear combination. Correspondingly, the variation of eigenpermittivities with frequency $\epsilon_m(\omega)$ can be obtained to arbitrary precision. Work in this direction is currently under way.

IV. IMPLEMENTATION AND NUMERICAL EXAMPLES

In practical terms, the key step in using GENOME is finding the eigenmodes and their eigenvalues. In this section, we describe some possible numerical implementations for the eigenmodes, before proceeding to detail our COMSOL MULTIPHYSICS implementation. We present some example eigenpermittivity modes produced by COMSOL MULTIPHYSICS. We then use these eigenmodes to expand the Green's tensor of the structure, thereby demonstrating GENOME. Finally, we compare GENOME with an incomplete naive modal expansion that also uses eigenpermittivity modes, demonstrating that only GENOME reproduces the real and imaginary parts of the Green's tensor correctly.

The linear eigenvalue equation for our modes is defined by Eq. (9) in integral form. Since the kernel of Eq. (9) is the Green's tensor of a uniform medium, the integral takes the form of a convolution, so efficient Fourier-domain solutions are possible. However, the eigenmode equation need not be solved in integral form, and the differential form can be used instead,

$$\nabla \times (\nabla \times \boldsymbol{E}_m) - \epsilon_b k^2 \boldsymbol{E}_m = \frac{1}{s_m}\theta(\boldsymbol{r}) k^2 \boldsymbol{E}_m, \tag{29}$$

obtained from Eq. (5) by setting $\boldsymbol{J} = 0$. This is the form we use for implementation in COMSOL MULTIPHYSICS. Additionally, simple structures such as spheres, slabs, and infinite cylinders admit analytic solutions via their well-known step-index dispersion relations [30,31,50]. In particular, we have recently applied the argument-principle method to the step-index fiber dispersion relation, enabling its efficient and robust solution [50]. The supplied code can also easily be adapted to solve other transcendental equations.

Finally, Eq. (9) can be efficiently solved for clusters of inclusions using the eigenmodes of its constituents as a basis. This exploits the fact that $\bar{\bar{G}}_0(|\boldsymbol{r} - \boldsymbol{r}'|)$ is common to all inclusions, even if they have different shapes or compositions, while $\theta(\boldsymbol{r}')$ is nonzero only inside the inclusions [30]. The procedure then amounts to evaluating overlap integrals between known modes and diagonalizing a small dense matrix. Rapid convergence is obtained because a complete set of modes is being used to represent another mode, all of which are smooth functions. Previous demonstrations include using modes of a sphere to generate modes of arbitrary clusters [30], and periodic arrays [29,42]. Completeness over all space is necessary for the success of this procedure. This procedure bears similarities to "perturbative" methods such as resonant-state expansion [9,46,62], which uses known complex frequency modes of a simple inclusion to generate modes of any enclosed inclusion [46]. Completeness of quasinormal modes inside the inclusion ensures that the series always converges for "perturbations" of any depth. In this regard, our procedure is analogous, but is applicable to "perturbations" both within the inclusion and of the background.

A. COMSOL MULTIPHYSICS Implementation

COMSOL MULTIPHYSICS is a commercial numerical simulation package for the finite-element method. We choose COMSOL MULTIPHYSICS for our eigenmode solver to demonstrate its ease of implementation on a widely used platform. COMSOL MULTIPHYSICS features an inbuilt eigenmode solver designed for complex eigenfrequency modes (27). However, this solver is easily repurposed to solve for eigenpermittivity modes, reexpressed in differential form as Eq. (29). This is accomplished via a substitution trick, eventually allowing the eigenfrequencies found by COMSOL MULTIPHYSICS to be reinterpreted as s_m. Furthermore, the eigenmodes found by COMSOL MULTIPHYSICS are the true eigenpermittivity modes.

More specifically, we define a simulation material to act as the background medium, set to have an artificial frequency-dependent permittivity

$$\tilde{\epsilon}_b(\tilde{k}) := \epsilon_b \frac{k^2}{\tilde{k}^2}, \tag{30}$$

where the tilde denotes COMSOL MULTIPHYSICS simulation variables, while ϵ_b and k are fixed simulation input parameters. This ensures the equality $\tilde{\epsilon}_b \tilde{k}^2 = \epsilon_b k^2$, or in other words, the simulation propagation constant remains equal to the desired propagation constant $\sqrt{\epsilon_b}k$ regardless of the COMSOL MULTIPHYSICS eigenfrequency. Note that $\tilde{k}^2$ may become complex during COMSOL MULTIPHYSICS's eigenvalue search, even if the parameters ϵ_b and k^2 are real. In this case, $\tilde{\epsilon}_b$ also becomes complex, so the product $\tilde{\epsilon}_b \tilde{k}^2$ remains real and the far-field behavior is always that of a passive lossless medium. Secondly, we define a simulation material to act as the scatterer, with permittivity unity:

$$\tilde{\epsilon}_i := 1. \tag{31}$$

This choice allows the eigenpermittivity to be identified via the equality $\tilde{\epsilon}_i \tilde{k}^2 = \epsilon_m k^2$, thus yielding

$$\epsilon_m = \frac{\tilde{k}^2}{k^2}. \tag{32}$$

Turning to other simulation considerations, an adaptive mesh with finer resolution near the surface is desirable. This enables greater accuracy when finding the plasmonic modes, which have evanescent fields. We also enclose the simulation domain with perfectly matched layers to reduce unwanted reflection. But this is not necessary, unlike with quasinormal modes, since our generalized normal modes are well behaved at infinity. Thus, it is possible to forgo the use of perfectly matched layers in generating the modes if their implementation is difficult. For example, we have also sucessfully generated the modes of Fig. 3 using instead the inbuilt scattering boundary conditions of COMSOL MULTIPHYSICS.

Once found, the eigenmodes $\boldsymbol{E}_m$ require normalization according to Eq. (16) before use. This is accomplished by numerically evaluating $\boldsymbol{E}_m \cdot \boldsymbol{E}_m$ across the interior of the inclusion using the inbuilt integration function, yielding the normalization constant. As discussed in Appendix A, this integral can evaluate to zero for symmetry reasons, especially for analytic eigenmodes constructed with cylindrical or spherical harmonics. While this can be easily remedied, it was unnecessary since in our experience COMSOL MULTIPHYSICS already generates modes with nonzero normalization integrals, even for highly symmetric inclusions, such as cylinders. This is true even if no attempt is made to incorporate the symmetry of the inclusion into the simulation using symmetric boundary conditions.

With the eigenmodes in hand, use of GENOME (26) proceeds by evaluating the detuning factors and adding the known $\bar{\bar{G}}_0(|\boldsymbol{r} - \boldsymbol{r}'|)$ term for a point source, finally plotting the fields as desired. These steps were performed using MATLAB, interfacing with COMSOL MULTIPHYSICS via LiveLink.

B. An alternative naive expansion

To demonstrate the importance of completeness, and thus use of the Lippmann-Schwinger equation in constructing GENOME, we first introduce an alternative naive expansion based on eigenpermittivity modes. Here we expand $\bar{\bar{G}}(\boldsymbol{r}, \boldsymbol{r}')$ directly in terms of the modes (9), with some coefficient $\boldsymbol{\alpha}_m(\boldsymbol{r}')$,

$$\bar{\bar{G}}(\boldsymbol{r}, \boldsymbol{r}') \approx \sum_m \boldsymbol{\alpha}_m(\boldsymbol{r}') \otimes \boldsymbol{E}_m(\boldsymbol{r}). \tag{33}$$

Implicit to this expansion is the false assumption that our eigenmodes are complete everywhere. Inserting Eq. (33) into Eq. (1) and projecting using the biorthogonality of eigenpermittivity modes, we arrive at the naive, erroneous expansion

$$\bar{\bar{G}}(\boldsymbol{r}, \boldsymbol{r}') \approx \frac{1}{k^2} \sum_m \frac{\boldsymbol{E}_m(\boldsymbol{r}) \otimes \boldsymbol{E}_m^\dagger(\boldsymbol{r}')}{\epsilon_m - \epsilon_i}, \tag{34}$$

which is not valid when the source $\boldsymbol{r}'$ is placed in the background. Analogous assumptions and procedures are sometimes employed by other expansion methods (e.g., when quasinormal modes are used). The performance of Eq. (34) is compared with that of Eq. (26) in the following subsection.

C. Numerical examples

Before proceeding to the COMSOL MULTIPHYSICS examples, we first demonstrate the capabilities of GENOME on a cylindrical scatterer of infinite extent in the third dimension. This is effectively a 2D geometry for which analytic solutions are available. Firstly, we generated a set of eigenpermittivity modes using the step-index fiber-dispersion relation [50]. To confirm GENOME, Eq. (26), we compared results against a direct calculation using cylindrical Mie theory, expanding the fields of a point source using Graf's addition theorem [81]. As demonstrated in Fig. 1, agreement was obtained, improving as more modes were included.

The metric we employed is a pseudo-L_2-norm of the relative difference, separating the real and imaginary parts. For example, for the real part we define, using the

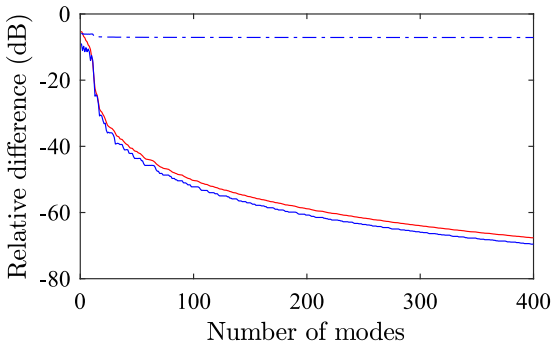

FIG. 1. An L_2 norm of the relative difference between cylindrical Mie theory and either GENOME or a naive expansion (34). The simulation geometry is similar to that in Fig. 2, except the inclusion is circular. Its diameter is $\lambda/4$, with permittivity $\epsilon_i = 12$. An in-plane point source is situated $\lambda/20$ from the circumference of the inclusion, oriented parallel to the surface. The relative difference of the real (red)and imaginary (blue) parts is shown. Convergence of GENOME (solid lines) continues to improve, while the naive expansion (dash-dotted lines) quickly saturates. Data for the real part of the naive expansion are not shown, as the integral diverges and is meaningless.

decibel scale,

$$\Delta\mathrm{Re}(G) = 10\log_{10}\left[\frac{\int \mathrm{Re}(G_{xy} - G_{xy,\mathrm{ref}})^2 + \mathrm{Re}(G_{yy} - G_{yy,\mathrm{ref}})^2 dA}{NA}\right]^{1/2}, \tag{35}$$

where the reference is taken to be the Mie solution, A is the area of the integration domain, and N is a normalization factor taken to be the maximum square modulus of the imaginary part of the Mie solution. A similar definition applies to the imaginary part, using the same value of N. The integration domain is a square twice the width of the cylinder but excluding the interior of the inclusion. This choice of domain was arbitrary, and the domain could be extended to infinity, since our expansion does not suffer from divergences there. However, this extension would dilute the discrepancy between GENOME and the reference Mie simulation, and would not give useful results. Integrals were approximated using the midpoint rule.

To ensure a fair comparison, the same angular orders were used for both GENOME and Mie-theory simulations, ranging from $m = -5$ to $m = 5$. Rapid agreement up to -30 dB was attained when only a few modes were included. Agreement continued to improve, increasing to -70 dB in all cases tested, which was achieved after 400 modes. Similar accuracy was achieved for both the real part and the imaginary part, even though the real part is divergent at the source location. Indeed, arbitrary accuracy is attainable, providing a numerical demonstration of the completeness of GENOME for exterior sources. Although the example shown involves a dielectric inclusion ($\epsilon_i = 12$), very similar convergence behavior was observed for lossy metallic inclusions. We also tested sources positions placed further from the cylinder. Slightly better performance is obtained, since the convergence curve is initially steeper.

For comparison purposes, the alternative expansion method, described in Sec. IV B, was also benchmarked. The naive expansion (34) uses the same set of modes but the expansion is not complete, so its accuracy quickly saturates and never improves. Furthermore, the accuracy of the real part is poor, since the naive expansion is unable to reproduce the $1/r^2$ divergence in the real part of the Green's tensor.

We proceed to demonstrate our COMSOL MULTIPHYSICS implementation of GENOME using a simple but nontrivial geometry, an inclusion with a triangular cross section shown in Fig. 2 and infinitely extending in the third dimension. Its corners have been rounded to avoid unphysical fields that would otherwise arise from geometric singularities. The inclusion size is $\lambda/4$, which is subwavelength, but not small enough such that an electrostatic treatment would suffice. This choice serves to showcase GENOME as an electrodynamic tool. Note that choosing the inclusion size is equivalent to fixing the frequency of operation, since material dispersion is irrelevant to eigenpermittivity modes, which separate geometric properties from material properties.

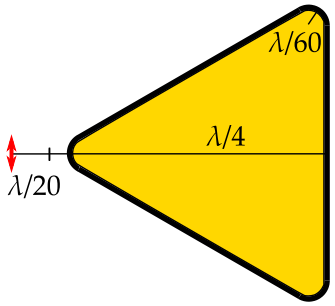

FIG. 2. The simulated inclusion geometry, an equilateral triangle with rounded corners. Its height is $\lambda/4$ from the base to the imaginary unrounded apex, while the radius of the rounded segments is $\lambda/60$. The point-dipole source is offset by $\lambda/20$ from the imaginary apex, with its position indicated by the double headed arrow, and its orientation parallel to the arrows.

Two types of symmetry are relevant to our chosen structure. Firstly, the 2D nature of the geometry separates all modes into strictly transverse magnetic or transverse electric polarizations. Secondly, the inclusion belongs to the C_{3v} point group, which has three irreducible representations, A_1, A_2, and E, of which E has a twofold degeneracy. In generating the eigenmodes, we chose not to incorporate any of these symmetries into the simulation. Nevertheless, COMSOL MULTIPHYSICS produces eigenmodes with either in-plane or out-of-plane fields that are zero to within numerical noise. Furthermore, COMSOL MULTIPHYSICS naturally recognizes modes of degenerate pairs when a fine enough mesh is used.

We now present some representative eigenpermittivity modes found by COMSOL MULTIPHYSICS. We categorize all modes into two types. The first we denote as plasmonic modes, typically with eigenpermittivities $\mathrm{Re}(\epsilon_m) < 0$. These have evanescent fields concentrated along the inclusion surface. The second type are dielectric modes, with $\mathrm{Re}(\epsilon_m) > 0$, and field distributions more typical of a finite potential well. There are an infinite number of both types of modes.

The lowest-order plasmonic modes are shown in Figs. 3(a)–3(c), along with their eigenpermittivities. $\mathrm{Im}(\epsilon_m)$ of the fundamental plasmonic mode is larger than that of the higher-order modes, indicating that it is a bright mode and the others are dark. All plasmonic modes shown are members of the E representation of the C_{3v} group, and are thus excited by in-plane dipole moments. Higher-order plasmonic modes feature progressively more nodes along the surface of the inclusion. Inclusion of more modes within GENOME gives better quantitative agreement,

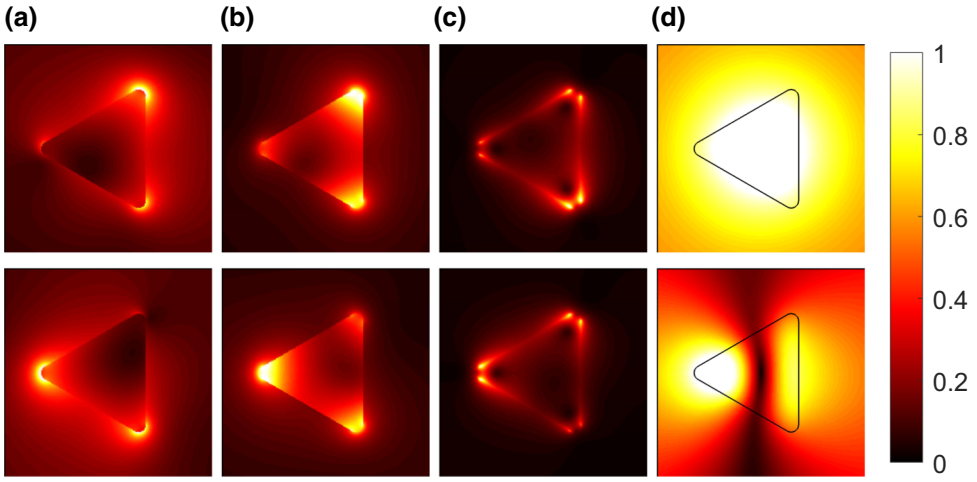

FIG. 3. (a)–(c) A degenerate member of a pair of plasmonic modes, along with their common eigenpermittivity. Since the fields of these modes are concentrated along the inclusion interface, the location of this interface is well delineated by the fields themselves. (d) The first two dielectric modes, with their respective eigenpermittivities. Here we superimpose an outline of the triangular inclusion. All plots show $|\boldsymbol{E}|$ in arbitrary units. Eigenpermittivities of the modes are (a) $\epsilon_m = -2.7 - 1.3i$, (b) $\epsilon_m = -0.46 - 0.13i$, (c) $\epsilon_m = -0.87 - 0.04i$, and (d) $\epsilon_m = 2.4 - 2.7i$, $\epsilon_m = 11.7 - 2.5i$.

especially for expansion of the real part of the Green's function, and particularly when the source point is close to the surface. Progressively higher-order modes have eigenpermittivities that asymptotically approach $\epsilon_m = -1$, which represents an accumulation point for the eigenvalue equation (9) [29,31]. In particular, the imaginary parts of their eigenpermittivities become infinitesimal, indicating that they are nonradiative. Their contributions to GENOME also become increasingly negligible because their fields are increasing confined to the inclusion surface, and so have little overlap with any excitation.

The first two dielectric modes are also shown in Fig. 3(d). The first mode belongs to the A_1 representation, and is thus excited by an out-of-plane dipole moment. The second mode belongs to the E representation, and is a member of a degenerate pair (not shown). Higher-order dielectric modes have more nodes, both in the radial direction and in the azimuthal direction. They also have larger positive $\mathrm{Re}(\epsilon_m)$, so their contributions to GENOME become increasingly small as they become detuned from any realistic inclusion permittivity.

We now demonstrate the use of these modes within GENOME via Eq. (26). We provide three examples, with inclusion permittivities of $\epsilon_i = 12$, $\epsilon_i = -2.70 + 3.55i$, and $\epsilon_i = -2.70$, all relying on the same modes. The first example places the scatterer close to a dielectric mode, while the latter two examples are "on resonance" with the bright plasmonic mode. To produce plots, we choose to locate the source dipole near the leftmost tip of the triangular inclusion and orient its moment along y, as shown in Fig. 2. This means we in fact use Eq. (25), plotting the components of the resulting $|E\rangle$ separately.

To proceed, we first obtain the field due to a line dipole in free space, representing $|E_0\rangle$. Since this is not frequently encountered in the literature, we devote Appendix B to its derivation. Then the contributions of the modes are summed according to their weights given in Eq. (25). The resulting E_x and E_y fields thus represent G_{xy} and G_{yy}, and are plotted in Figs. 4–6, showing both real and imaginary parts. We chose a dipole strength of $\boldsymbol{p}/\epsilon_0 = 1$ V m, where $\boldsymbol{p}$ is the dipole moment per unit length in the perpendicular direction, oscillating at frequency $\omega/c = 1$ m^{-1} in a vacuum background. This choice of units allows the figures to simultaneously represent the electric field, in the unit of volts per meter, and the Green's tensor, which is a unitless quantity in two dimensions.

To provide a benchmark for GENOME, we plot a direct simulation of a radiating dipole source produced by COMSOL without using any eigenmode expansion. Also plotted is the result of the naive expansion described in Sec. IV B. The spatially resolved difference between the direct simulation and the two expansions is plotted in Fig. 7. Out-of-plane electric fields are not shown, as they are of the order 10^{-8}, representing numerical noise.

Figure 4 shows the simulation of the $\epsilon_i = 12$ inclusion. The dominant pair of modes excited is the second mode in Fig. 3(d), with eigenpermittivity $\epsilon_m = 11.7 - 2.5i$, and its partner (not shown). As demonstrated in Fig. 4 and the first row in Fig. 7, GENOME obtains quantitative agreement with the benchmark direct simulation, reproducing both the real part and the imaginary part of the Green's tensor. Graphical accuracy is obtained, and in particular, the agreement of the imaginary parts [Figs. 4(c) and 4(d)]

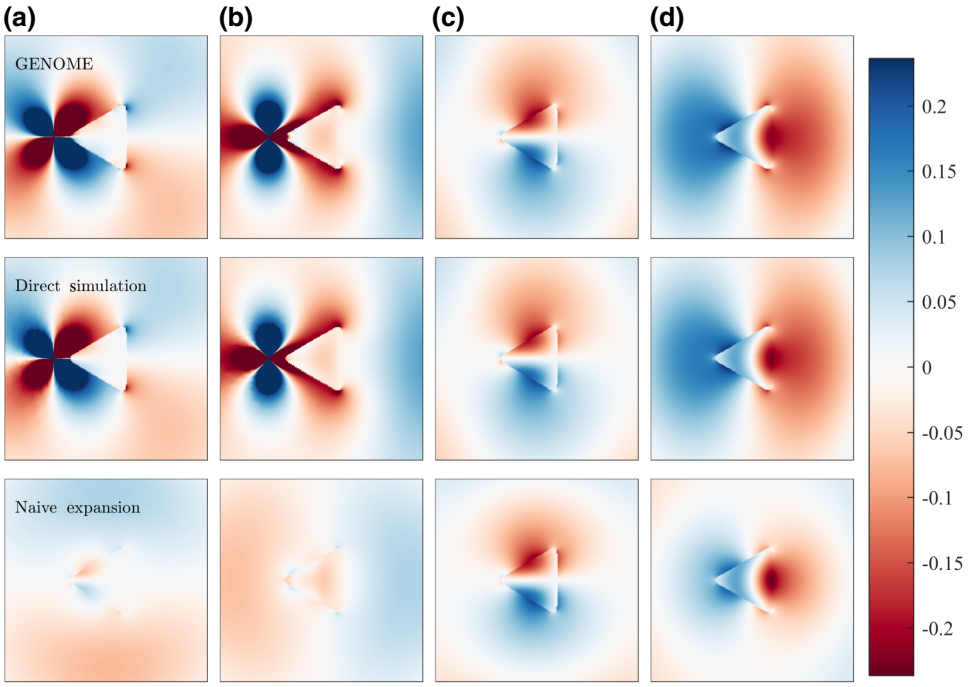

FIG. 4. Three different simulation methods of an identical geometry, with an x-oriented dipole placed near a triangular inclusion of $\epsilon_i = 0.87$. The first row shows the results of GENOME, the second row shows direct COMSOL MULTIPHYSICS simulation with a point source, and the third row shows the naive expansion (34) derived in Sec. IV B. The scaling is identical between each row. Each column displays a different component of Green's tensor, corresponding to (a) $\mathrm{Re}(G_{xy})$, (b) $\mathrm{Re}(G_{yy})$, (c) $\mathrm{Im}(G_{xy})$, and (d) $\mathrm{Im}(G_{yy})$. We omit the outline of the inclusion from Fig. 3(d) as the location of the boundary is clear from the fields themselves.

is better than 2% throughout the domain. The agreement of the real parts is not as consistently good, but the disagreement is mostly localized to the region around the source. The speckled nature of the error here, visible in Fig. 7(a), suggests that it originates from the direct COMSOL MULTIPHYSICS simulation, specifically, the difficulty of reproducing the singularity using a piecewise polynomial basis on a triangular mesh. In other words, GENOME is likely to be more accurate than our benchmark since the singularity is handled analytically as part of $\bar{\bar{G}}_0$ in Eq. (26).

In all plots, 50 modes were included in the expansions, including 11 plasmonic modes. We show in Fig. 8 the convergence as a function of the number of modes, using the same metric (35) as in Fig. 1. The integration domain is now the whole visible domain in Figs. 4–7. However, we plot only the difference in the imaginary parts, since the difference in the real parts is likely to be dominated by the aforementioned errors of the direct COMSOL MULTIPHYSICS simulation. The agreement between GENOME and the benchmark begins to saturate, so only data up

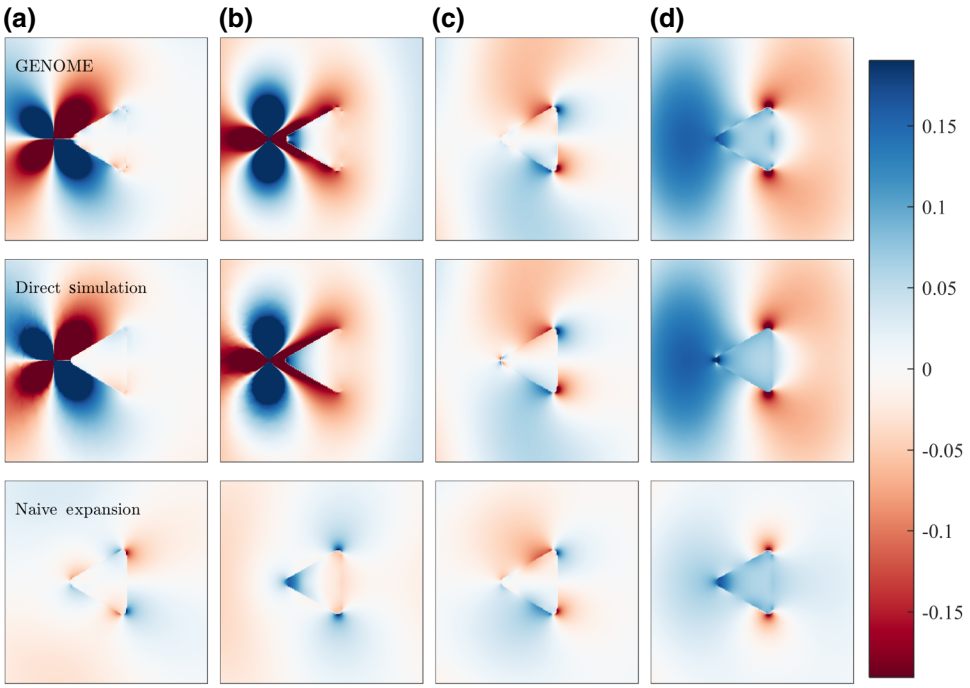

FIG. 5. As in Fig. 4, but the permittivity of the triangular inclusion is $\epsilon_i = -2.70 + 3.55i$. Columns show (a) $\mathrm{Re}(G_{xy})$, (b) $\mathrm{Re}(G_{yy})$, (c) $\mathrm{Im}(G_{xy})$, and (d) $\mathrm{Im}(G_{yy})$.

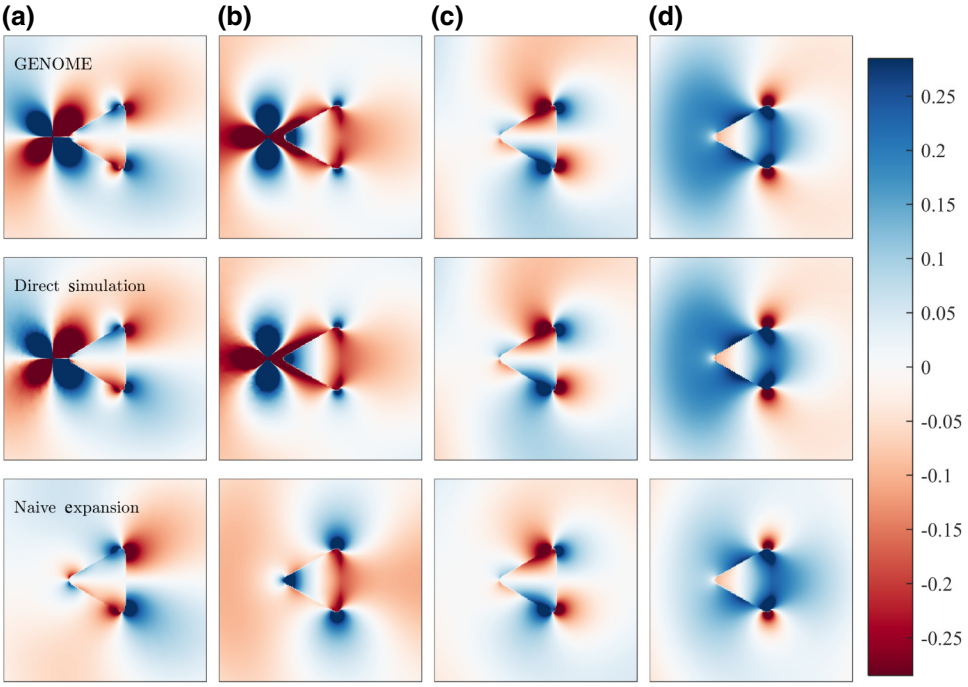

FIG. 6. As in Fig. 4, but the permittivity of the triangular inclusion is $\epsilon_i = -2.70$. Columns show (a) $\mathrm{Re}(G_{xy})$, (b) $\mathrm{Re}(G_{yy})$, (c) $\mathrm{Im}(G_{xy})$, and (d) $\mathrm{Im}(G_{yy})$.

to 25 modes are plotted. This contrasts with the analytic results in Fig. 1, where the agreement continues to improve. The saturation is likely due to numerical errors in the direct COMSOL MULTIPHYSICS simulation, the COMSOL MULTIPHYSICS generated modes, or both.

We now compare the naive expansion (34) with the direct simulation. The first notable difference is that the singularity in the real part of Green's tensor is not correctly reproduced. As seen in Fig. 7(b), the disagreement is at least of the order of unity across large portions of the plot domain, even far away from the source. The agreement is also poor for the imaginary parts, where the weighted average discrepancy is approximately 26%, as seen in Fig. 8. Indeed, the large quantitative discrepancy leads to noticeable qualitative discrepancies, particularly in the $\mathrm{Im}(G_{yy})$ component.

For the metallic example, we chose an inclusion permittivity of $\epsilon_i - 2.7 + 3.55i$, corresponding to gold at 502 nm, according to Johnson and Christy data. The inclusion is thus approximately "on resonance" with the bright

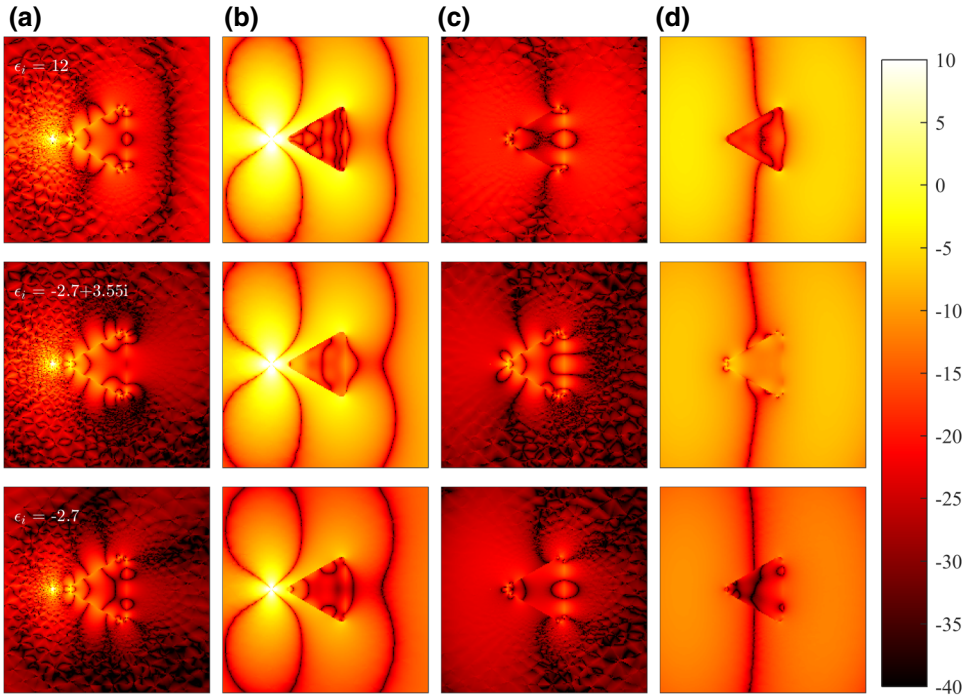

FIG. 7. Shows the relative difference between direct COMSOL MULTIPHYSICS simulation and expansion via either GENOME or the naive expansion. The metric used is similar to Eq. (35), but shows instead the spatially resolved relative difference of the G_{yy} component on a decibel scale. Each row corresponds to a different set of simulations, with the first row corresponding to Fig. 4, the second row corresponding to Fig. 5, and the third row corresponding to Fig. 6. Only differences in G_{yy} are shown, arranged into columns corresponding to (a) $\mathrm{Re}(G_{yy})$, (b) $\mathrm{Re}(G_{yy})$, (c) $\mathrm{Im}(G_{yy})$, and (d) $\mathrm{Im}(G_{yy})$.

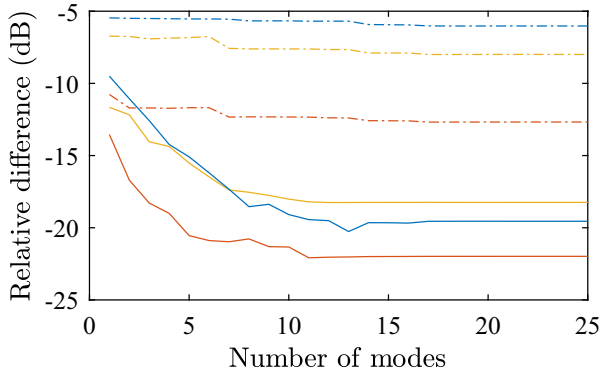

FIG. 8. As in Fig. 1, but an L_2 norm of the relative difference between the imaginary parts of direct COMSOL MULTIPHYSICS simulation and either GENOME (solid lines) or the naive expansion (dash-dotted lines). Blue lines are for inclusion permittivity $\epsilon_i = 12$, yellow lines are for $\epsilon_i = -2.7 + 3.55i$, and red lines are for $\epsilon_i = -2.7$, corresponding, respectively, to Figs. 4, 5, and 6.

modes of Fig. 3(a), with eigenpermittivity $\epsilon_m = -2.7 - 1.3i$. However, the radiative nature of this pair of modes means that they have a relatively large negative $\mathrm{Im}(\epsilon_m)$, so their detuning from a passive medium can never be arbitrarily small. Consequently, the bright pair of modes is not dominant, and their contribution is roughly equal to that of the next dominant pair. As seen in Fig. 5, we observe agreement similar to that of our dielectric example, obtaining graphical accuracy compared with the benchmark direct simulation. This is also demonstrated in Fig. 7, where agreement in the imaginary parts is good across the domain, while the agreement in the real part is good except near the source. As before, large discrepancies are observed when the naive expansion is used, particularly the real parts and the $\mathrm{Im}(G_{yy})$ component.

Finally, we show in Fig. 6 the effect of artificially neglecting loss by simulating an inclusion of permittivity $\epsilon_i - 2.7$. Consequently, the inclusion is brought closer to the resonance, $\epsilon_m = -2.7 - 1.3i$, so its contribution to the expansion is more dominant. As seen in Figs. 7 and 8, an improvement in the performance of GENOME is observed. However, more remarkable is the improvement of the naive expansion, with the average discrepancy in the imaginary part dropping to 4%, though some qualitative differences in $\mathrm{Im}(G_{yy})$ remain. This example helps to demonstrate that the naive expansion is incomplete, as somewhat satisfactory results from Eq. (34) can be obtained only if a single on-resonance mode is dominant. This is demonstrated by Fig. 8 and supported by the analytic results in Fig. 1, where it can be seen that none of the subsequent, more detuned modes improve the convergence. The success of the analogous quasinormal mode expansion, which is also incomplete for exterior sources, can be explained in such terms, as it is well suited to situations where a handful of on-resonance modes are dominant. Conversely, GENOME continues to converge as more modes are considered, so the modal completeness of GENOME ensures accuracy regardless of whether the structure is on resonance or detuned from resonance.

V. SUMMARY

In this paper, we develop GENOME, a modal expansion for the electromagnetic Green's tensor based on stationary normal modes generalized to handle lossy resonators in open systems. Its foundation is the Lippmann-Schwinger equation, Eq. (7), introduced in Sec. II A. Expansion proceeds using eigenmodes of the Lippmann-Schwinger equation, defined in Sec. II B. Crucially, we define the permittivity of the inclusion as the eigenvalue, resulting in the linear eigenvalue equation (9). Physical interpretations of eigenpermittivity modes and some of their properties are also discussed in Sec. II B. The expansion itself is derived in Sec. IIC, culminating in the final GENOME expression (26).

Since GENOME uses true normal modes, it has a number of advantages, as discussed in Sec. III. The modes remain discrete and are biorthogonal, which greatly facilitates modal expansion. The modes are complete, ensuring that the expansion always converges toward the true solution of the target inhomogeneous differential equation (4). This remains true for the far fields, where our modes intrinsically satisfy the governing source-free differential equation, thus simultaneously obeying Sommerfeld boundary conditions and decaying to zero. This has the additional benefit of trivializing normalization. We describe numerical implementation of GENOME in Sec. IV, focusing on the key step of generating the eigenpermittivity modes. Since the defining eigenvalue equation is linear, several possibilities are described. In particular, preexisting eigenmode solvers can be adapted with a simple substitution trick, described in Sec. IV A. In Sec. IV B, we present results from our COMSOL MULTIPHYSICS implementation, based on the differential form of the defining eigenmode equation (29). We obtain the modes of a triangular inclusion, and provide some further discussion on the characteristics of eigenpermittivity modes. We then proceed to use these modes in GENOME, comparing our expansion with a direct COMSOL MULTIPHYSICS simulation of a point source. Graphical accuracy in the radiated fields is obtained, particularly for the imaginary part. Finally, we demonstrate the importance of completeness by comparing GENOME with a naive expansion that also uses eigenpermittivity modes, Eq. (34), that never converges toward the true solution, regardless of the number of modes used.

ACKNOWLEDGMENTS

We thank A. Farhi, P. Lallane, and K. Vynck for many useful discussions. P.Y.C. and Y.S. were partially

supported by the Israel Science Foundation (Grant No. 899/16) and the Israeli National Nanotechnology Initiative.

APPENDIX A: ADJOINT MODES

We now give the explicit forms for the overlap integrals in Eq. (21),

$$\langle E_m|\hat{\theta}|E_0\rangle = \int \theta(\boldsymbol{r})\boldsymbol{E}_m^{\dagger}(\boldsymbol{r})\cdot\boldsymbol{E}_0(\boldsymbol{r})d\boldsymbol{r}, \tag{A1}$$

and in Eq. (25),

$$\langle E_m|J\rangle = \int \boldsymbol{E}_m^{\dagger}(\boldsymbol{r})\cdot\boldsymbol{J}(\boldsymbol{r})d\boldsymbol{r}. \tag{A2}$$

The adjoint field $\boldsymbol{E}_m^{\dagger}(\boldsymbol{r})$ in Eqs. (A1) and (A2) is not necessarily the complex-conjugate field $\boldsymbol{E}_m^{*}(\boldsymbol{r})$, which is the familiar form of $\langle E_m|$ for a self-adjoint or Hermitian operator. Instead, the operator $\hat{\Gamma}\hat{\theta}$ in Eq. (13) is symmetric, so the adjoint field is identical to the direct field [30]:

$$\boldsymbol{E}_m^{\dagger}(\boldsymbol{r}) = \boldsymbol{E}_m(\boldsymbol{r}). \tag{A3}$$

Equation (A3) is true unless the structure itself possesses symmetry. For example, an infinite cylinder has both continuous translational symmetry and continuous rotational symmetry, giving rise to $e^{i\beta z}$ and $e^{im\theta}$ variations in the respective directions. In this case, Eq. (A3) must be modified, and the adjoint field is obtained by the substitutions $\beta\rightarrow-\beta$ and $m\rightarrow-m$, while leaving the radial variation of the mode unchanged [7,30,31,72]. Alternatively, the modes may be constructed using sine and cosine linear combinations of $e^{\pm i\beta z}$ and $e^{\pm im\theta}$, and Eq. (A3) once again becomes true [7,9,72].

APPENDIX B: FIELDS OF A LINE DIPOLE

We aim to obtain the fields radiated by a line-dipole source, which is of infinitesimal extent in two dimensions but is infinite in extent in the third dimension. The line dipole is defined by its components $\boldsymbol{p}=(p_x;p_y;p_z)$, with dimension of dipole moment per unit length. The line dipole may have harmonic $e^{i\beta z}$ variation along the third dimension.

To derive the dipole fields, we proceed via the Green's tensor of free space, defined by Eq. (1), which is related to the Green's scalar for the Helmholtz equation by the well known relation

$$\bar{\bar{G}}_0(r) = \left(\bar{\bar{I}} + \frac{1}{k^2}\nabla\nabla\right)G_0(r), \tag{B1}$$

where without loss of generality, we have placed the source at the coordinate origin, so r itself represents the distance separation. Furthermore, the background permittivity ϵ may simply be absorbed into k^2. For our 2D geometry,

$$\nabla = \nabla_{\perp} + i\beta\hat{\boldsymbol{z}}, \tag{B2}$$

where $\nabla_{\perp}$ applies only to the in-plane directions. The appropriate Green's scalar is the 2D version,

$$G_0(r) = \frac{i}{4}H_0(\alpha r), \tag{B3}$$

where α is the in-plane propagation constant, $\alpha^2+\beta^2=k^2$.

In explicit form, the nine components of Green's tensor in Cartesian form are

$$\bar{\bar{G}}(r) = \frac{1}{k^2}\begin{bmatrix} k^2+\partial_x^2 & \partial_x\partial_y & i\beta\partial_x \\ \partial_y\partial_x & k^2+\partial_y^2 & i\beta\partial_y \\ i\beta\partial_x & i\beta\partial_y & \alpha^2 \end{bmatrix}\frac{i}{4}H_0(\alpha r). \tag{B4}$$

However, it is more convenient to evaluate the derivatives in polar coordinates (r,θ), so the chain rule is used to obtain

$$\partial_x = (\partial_x r)\partial_r = \cos\theta\,\partial_r, \quad \partial_y = (\partial_y r)\partial_r = \sin\theta\,\partial_r, \tag{B5}$$

where derivatives corresponding to ∂_θ may be neglected since $H_0(\alpha r)$ is invariant with θ. Second derivatives are similarly obtained, though this time ∂_θ cannot be ignored. Next the Cartesian unit vectors should also be transformed into cylindrical unit vectors, with the usual transformation matrix. However, the cylindrical unit vectors are not appropriate for sources located at the coordinate origin, where they are not well defined. Instead, we introduce the rotational or angular momentum unit vectors

$$\hat{\boldsymbol{e}}_+ = \frac{1}{2}(\hat{\boldsymbol{x}}+i\hat{\boldsymbol{y}}), \quad \hat{\boldsymbol{e}}_- = \frac{1}{2}(\hat{\boldsymbol{x}}-i\hat{\boldsymbol{y}}), \tag{B6}$$

so the dipole moments instead have the components $(p_+;p_-;p_z)$. Application of these transformations to Eq. (B4) yields

$$\bar{\bar{G}}(r) = \frac{1}{k^2}\begin{bmatrix} \beta^2-\frac{1}{r}\partial_r & \beta^2-\frac{1}{r}\partial_r & i\beta\partial_r \\ -i\left(k^2+\frac{1}{r}\partial_r\right) & i\left(k^2+\frac{1}{r}\partial_r\right) & 0 \\ i\beta\partial_r & i\beta\partial_r & \alpha^2 \end{bmatrix} \times \begin{bmatrix} e^{-i\theta} & 0 & 0 \\ 0 & e^{i\theta} & 0 \\ 0 & 0 & 1 \end{bmatrix}\frac{i}{4}H_0(\alpha r). \tag{B7}$$

In arriving at Eq. (B7), simplifications were performed using Bessel-function identities.

Alternatively, in two dimensions it is sufficient to specify the fields using E_z and H_z alone, from which all other field components can be derived using the Maxwell curl

equations. The E_z field produced by a line dipole can be calculated using Eq. (3) with the explicit form (B7) to yield

$$E_z = \frac{\alpha}{4\epsilon_b}\left[i\alpha\frac{p_z}{\epsilon_0}H_0(\alpha r) - \beta\frac{p_+}{\epsilon_0}H_{-1}(\alpha r)e^{-i\theta} + \beta\frac{p_-}{\epsilon_0}H_1(\alpha r)e^{i\theta}\right]e^{i\beta z}, \tag{B8}$$

while the H_z field can be obtained from the curl of Eq. (B7) to yield

$$\sqrt{\frac{\mu_0}{\epsilon_0}}H_z = -\frac{i}{4}k\alpha\left[\frac{p_+}{\epsilon_0}H_{-1}(\alpha r)e^{-i\theta} + \frac{p_-}{\epsilon_0}H_1(\alpha r)e^{i\theta}\right]e^{i\beta z}, \tag{B9}$$

where we have restored ϵ_b, the background permittivity.

[1] Philip McCord Morse and Herman Feshbach, *Methods of Theoretical Physics* (Technology Press, Cambridge, Massachusetts, 1946).

[2] George B. Arfken and Hans J. Weber, *Mathematical Methods for Physicists* (Academic Press, Orlando, Florida, 2012).

[3] Lukas Novotny and Bert Hecht, *Principles of Nano-Optics* (Cambridge University Press, Cambridge, 2012).

[4] A. J. F. Siegert, On the derivation of the dispersion formula for nuclear reactions, Phys. Rev. **56**, 750 (1939).

[5] Carl E. Baum, On the Singularity Expansion Method for the Solution of Electromagnetic Interaction Problems, Type Tech. Rep. Number AFWL-88 (AIR FORCE WEAPONS LAB KIRTLAND AFBNM, AIR FORCE WEAPONS LAB KIRTLAND AFB NM, 1971).

[6] C. E. Baum, Emerging technology for transient and broadband analysis and synthesis of antennas and scatterers, Proc. IEEE **64**, 1598 (1976).

[7] H. M. Lai, P. T. Leung, K. Young, P. W. Barber, and S. C. Hill, Time-independent perturbation for leaking electromagnetic modes in open systems with application to resonances in microdroplets, Phys. Rev. A **41**, 5187 (1990).

[8] P. T. Kristensen, C. Van Vlack, and S. Hughes, Generalized effective mode volume for leaky optical cavities, Opt. Lett. **37**, 1649 (2012).

[9] M. B. Doost, W. Langbein, and E. A. Muljarov, Resonant state expansion applied to two-dimensional open optical systems, Phys. Rev. A **87**, 043827 (2013).

[10] C. Sauvan, J. P. Hugonin, I. S. Maksymov, and P. Lalanne, Theory of the Spontaneous Optical Emission of Nanosize Photonic and Plasmon Resonators, Phys. Rev. Lett. **110**, 237401 (2013).

[11] Y. Kantor and D. J. Bergman, Improved rigorous bounds on the effective elastic moduli of a composite material, J. Mech. Phys. Solids **32**, 41 (1984).

[12] Israel Cohen and David J. Bergman, Effective elastic properties of periodic composite medium, J. Mech. Phys. Solids **51**, 1433 (2003).

[13] Yehuda B. Band and Yshai Avishai, *Quantum Mechanics with Applications to Nanotechnology and Information Science* (Academic Press, Oxford, 2013)

[14] S. Chandrasekhar and S. Detweiler, The quasi-normal modes of the Schwarzschild black hole, Proc. R. Soc. Lond. Ser. Math. Phys. Sci. **344**, 441 (1975).

[15] P. T. Leung, Y. T. Liu, W.-M. Suen, C. Y. Tam, and K. Young, Quasinormal modes of Dirty Black Holes, Phys. Rev. Lett. **78**, 2894 (1997).

[16] R. Carminati, A. Cazé, D. Cao, F. Peragut, V. Krachmalnicoff, R. Pierrat, and Y. De Wilde, Electromagnetic density of states in complex plasmonic systems, Surf. Sci. Rep. **70**, 1 (2015).

[17] Vitaliy N. Pustovit and Tigran V. Shahbazyan, Plasmon-mediated superradiance near metal nanostructures, Phys. Rev. B **82**, 075429 (2010).

[18] Pierre Fauché, Christian Gebhardt, Maxim Sukharev, and Renaud A. L. Vallée, Plasmonic opals: Observation of a collective molecular exciton mode beyond the strong coupling, Sci. Rep. **7**, 4107 (2017).

[19] Willem L. Vos, A. Femius Koenderink, and Ivan S. Nikolaev, Orientation-dependent spontaneous emission rates of a two-level quantum emitter in any nanophotonic environment, Phys. Rev. A **80**, 053802 (2009).

[20] Navin A. R. Bhat and J. E. Sipe, Hamiltonian treatment of the electromagnetic field in dispersive and absorptive structured media, Phys. Rev. A **73**, 063808 (2006).

[21] E. S. C. Ching, P. T. Leung, A. Maassen van den Brink, W. M. Suen, S. S. Tong, and K. Young, Quasinormal-mode expansion for waves in open systems, Rev. Mod. Phys. **70**, 1545 (1998).

[22] K. M. Lee, P. T. Leung, and K. M. Pang, Dyadic formulation of morphology-dependent resonances. I. completeness relation, J. Opt. Soc. Am. B **16**, 1409 (1999).

[23] Philip Trøst Kristensen and Stephen Hughes, Modes and mode volumes of leaky optical cavities and plasmonic nanoresonators, ACS Photonics **1**, 2 (2014).

[24] C. Sauvan, J. P. Hugonin, R. Carminati, and P. Lalanne, Modal representation of spatial coherence in dissipative and resonant photonic systems, Phys. Rev. A **89**, 043825 (2014).

[25] E. A. Muljarov and W. Langbein, Exact mode volume and purcell factor of open optical systems, Phys. Rev. B **94**, 235438 (2016).

[26] Q. I. Dai, W. C. Chew, Y. H. Lo, Y. G. Liu, and L. J. Jiang, Generalized modal expansion of electromagnetic field in 2-D bounded and unbounded media, IEEE Antennas Wirel. Propag. Lett. **11**, 1052 (2012).

[27] P. T. Leung, S. Y. Liu, and K. Young, Completeness and orthogonality of quasinormal modes in leaky optical cavities, Phys. Rev. A **49**, 3057 (1994).

[28] David J. Bergman, Dielectric constant of a two-component granular composite: A practical scheme for calculating the pole spectrum, Phys. Rev. B **19**, 2359 (1979).

[29] D. J. Bergman, The dielectric constant of a simple cubic array of identical spheres, J. Phys. C: Solid State Phys. **12**, 4947 (1979).

[30] David J. Bergman and D. Stroud, Theory of resonances in the electromagnetic scattering by macroscopic bodies, Phys. Rev. B **22**, 3527 (1980).

[31] Asaf Farhi and David J. Bergman, Electromagnetic eigenstates and the field of an oscillating point electric dipole in a flat-slab composite structure, Phys. Rev. A **93**, 063844 (2016).

[32] Mikhail S. Agranovich, Boris Z. Katsenelenbaum, Aleksej N. Sivov, and Nikolai N. Voitovich, *Generalized Method of Eigenoscillations in Diffraction Theory* (Wiley-VCH, Berlin, New York, 1999), 1st ed.

[33] Titus Sandu, Eigenmodede composition of the near-field enhancement in localized surface plasmon resonances of metallic nanoparticles, Plasmonics **8**, 391 (2012).

[34] O. D. Miller, C. W. Hsu, M. T. H. Reid, W. Qiu, B. G. DeLacy, J. D. Joannopoulos, M. Soljačić, and S. G. Johnson, Fundamental Limits to Extinction by Metallic Nanoparticles, Phys. Rev. Lett. **112**, 123903 (2014).

[35] Owen D. Miller, Athanasios G. Polimeridis, M. T. Homer Reid, Chia Wei Hsu, Brendan G. DeLacy, John D. Joannopoulos, Marin Soljačić, and Steven G. Johnson, Fundamental limits to optical response in absorptive systems, Opt. Express **24**, 3329 (2016).

[36] David J. Bergman and Mark I. Stockman, Surface Plasmon Amplification by Stimulated Emission of Radiation: Quantum Generation of Coherent Surface Plasmons in Nanosystems, Phys. Rev. Lett. **90**, 027402 (2003).

[37] Kuiru Li, Mark I. Stockman, and David J. Bergman, Self-Similar Chain of Metal Nanospheres as an Efficient Nanolens, Phys. Rev. Lett. **91**, 227402 (2003).

[38] Mark I. Stockman, Sergey V. Faleev, and David J. Bergman, Localization Versus Delocalization of Surface Plasmons in Nanosystems: Can One State Have Both Characteristics? Phys. Rev. Lett. **87**, 167401 (2001).

[39] Mark I. Stockman, Sergey V. Faleev, and David J. Bergman, Coherent Control of Femtosecond Energy Localization in Nanosystems, Phys. Rev. Lett. **88**, 067402 (2002).

[40] Mark I. Stockman, David J. Bergman, Cristelle Anceau, Sophie Brasselet, and Joseph Zyss, Enhanced Second-Harmonic Generation by Metal Surfaces with Nanoscale Roughness: Nanoscale Dephasing, Depolarization, and Correlations, Phys. Rev. Lett. **92**, 057402 (2004).

[41] Kuiru Li, Mark I. Stockman, and David J. Bergman, Enhanced second harmonic generation in a self-similar chain of metal nanospheres, Phys. Rev. B **72**, 153401 (2005).

[42] David J. Bergman and Keh-Jim Dunn, Bulk effective dielectric constant of a composite with a periodic microgeometry, Phys. Rev. B **45**, 13262 (1992).

[43] David J. Bergman, Uri Evra, and Xiangting Li, *Radiative Life Times of Mano-Plasmonic States* (International Society for Optics and Photonics, 2005), p. 59270I.

[44] K. Nireekshan Reddy, Parry Y. Chen, Antonio I. Fernández-Domńguez, and Yonatan Sivan, Revisiting the boundary conditions for second-harmonic generation at metal-dielectric interfaces, J. Opt. Soc. Am. B **34**, 1824 (2017).

[45] Li Ge, Y. D. Chong, and A. Douglas Stone, Steady-state ab initio laser theory: Generalizations and analytic results, Phys. Rev. A **82**, 063824 (2010).

[46] M. B. Doost, W. Langbein, and E. A. Muljarov, Resonant-state expansion applied to three-dimensional open optical systems, Phys. Rev. A **90**, 013834 (2014).

[47] Robert S. Mulliken, Spectroscopy, molecular orbitals, and chemical bonding, Science **157**, 13 (1967).

[48] James E. Huheey, Ellen A. Keiter, and Richard L. Keiter, *Inorganic Chemistry: Principles of Structure and Reactivity* (Prentice Hall, New York, NY, 1997), 4th ed.

[49] E. Prodan, C. Radloff, N. J. Halas, and P. Nordlander, A hybridization model for the plasmon response of complex nanostructures, Science **302**, 419 (2003).

[50] Parry Y. Chen and Yonatan Sivan, Robust location of optical fiber modes via the argument principle method, Comput. Phys. Commun. **214**, 105 (2017).

[51] Edward M. Purcell and Carlton R. Pennypacker, Scattering and absorption of light by nonspherical dielectric grains, Astrophys. J. **186**, 705 (1973).

[52] Roger F. Harrington, *Field computation by moment methods* (IEEE Press, Piscataway, NJ, 1993).

[53] Akhlesh Lakhtakia, Macroscopic theory of the coupled dipole approximation method, Opt. Commun. **79**, 1 (1990).

[54] John David Jackson, *Classical Electrodynamics* (John Wiley & Sons, New York, 2007).

[55] Olivier J. F. Martin, Alain Dereux, and Christian Girard, Iterative scheme for computing exactly the total field propagating in dielectric structures of arbitrary shape, J. Opt. Soc. Am. A **11**, 1073 (1994).

[56] Philip Trst Kristensen, Peter Lodahl, and Jesper Mørk, Light propagation in finite-sized photonic crystals: Multiple scattering using an electric field integral equation, J. Opt. Soc. Am. B **27**, 228 (2010).

[57] Mark I. Stockman, Spaser Action, Loss Compensation, and Stability in Plasmonic Systems with Gain, Phys. Rev. Lett. **106**, 156802 (2011).

[58] Craig F. Bohren and Donald R. Huffman, *Absorption and Scattering of Light by Small Particles* (John Wiley & Sons, New York, 1983).

[59] Hollis C. Chen, *Theory of Electromagnetic Waves: A Coordinate-Free Approach* (McGraw-Hill, New York, 1983).

[60] Cristian L. Cortes and Zubin Jacob, Super-coulombic atom-atom interactions in hyperbolic media, Nat. Commun. **8**, ncomms14144 (2017).

[61] Claude Cohen-Tannoudji, Jacques Dupont-Roc, and Gilbert Grynberg, *Atom-Photon Interactions: Basic Processes and Applications* (Wiley-VCH, New York, 1998).

[62] E. A. Muljarov, W. Langbein, and R. Zimmermann, Brillouin-wigner perturbation theory in open electromagnetic systems, EPL **92**, 50010 (2010).

[63] Not to be confused with resonant-state expansion, which is a perturbation method using resonant states.

[64] Q. Bai, M. Perrin, C. Sauvan, J.-P. Hugonin, and P. Lalanne, Efficient and intuitive method for the analysis of light scattering by a resonant nanostructure, Opt. Express **21**, 27371 (2013).

[65] Rong-Chun Ge, Philip Trst Kristensen, Jeff F. Young, and Stephen Hughes, Quasinormal mode approach to modelling light-emission and propagation in nanoplasmonics, New J. Phys. **16**, 113048 (2014).

[66] Rong-Chun Ge and S. Hughes, Design of an efficient single photon source from a metallic nanorod dimer: A quasi-normal mode finite-difference time-domain approach, Opt. Lett. **39**, 4235 (2014).

[67] Jianji Yang, Harald Giessen, and Philippe Lalanne, Simple analytical expression for the peak-frequency shifts of plasmonic resonances for sensing, Nano Lett. **15**, 3439 (2015).

[68] Philippe Lalanne, Wei Yan, Kevin Vynck, Christophe Sauvan, and Jean-Paul Hugonin, Light interaction with photonic and plasmonic resonances, ArXiv:1705.02433 [Phys] (2017).

[69] Benjamin Vial, Frédéric Zolla, André Nicolet, and Mireille Commandré, Quasimodal expansion of electromagnetic fields in open two-dimensional structures, Phys. Rev. A **89**, 023829 (2014).

[70] P. T. Leung, S. Y. Liu, and K. Young, Completeness and time-independent perturbation of the quasinormal modes of an absorptive and leaky cavity, Phys. Rev. A **49**, 3982 (1994).

[71] E. A. Muljarov and W. Langbein, Resonant-state expansion of dispersive open optical systems: Creating gold from sand, Phys. Rev. B **93**, 075417 (2016).

[72] Philip Trøst Kristensen, Rong-Chun Ge, and Stephen Hughes, Normalization of quasinormal modes in leaky optical cavities and plasmonic resonators, Phys. Rev. A **92**, 053810 (2015).

[73] E. A. Muljarov and W. Langbein, Comment on "normalization of quasinormal modes in leaky optical cavities and plasmonic resonators," Phys. Rev. A **96**, 017801 (2017).

[74] Philip Trøst Kristensen, Rong-Chun Ge, and Stephen Hughes, Reply to "comment on 'normalization of quasinormal modes in leaky optical cavities and plasmonic resonators," Phys. Rev. A **96**, 017802 (2017).

[75] Philip Trøst Kristensen, Jakob Rosenkrantz de Lasson, and Niels Gregersen, Calculation, normalization, and perturbation of quasinormal modes in coupled cavity-waveguide systems, Opt. Lett. **39**, 6359 (2014).

[76] T. Weiss, M. Mesch, M. Schäferling, H. Giessen, W. Langbein, and E. A. Muljarov, From Dark to Bright: First-Order Perturbation Theory with Analytical Mode Normalization for Plasmonic Nanoantenna Arrays Applied to Refractive Index Sensing, Phys. Rev. Lett. **116**, 237401 (2016).

[77] T. Weiss, M. Schäferling, H. Giessen, N. A. Gippius, S. G. Tikhodeev, W. Langbein, and E. A. Muljarov, Analytical normalization of resonant states in photonic crystal slabs and periodic arrays of nanoantennas at oblique incidence, Phys. Rev. B **96**, 045129 (2017).

[78] Tatsuya Kashiwa and Ichiro Fukai, A treatment by the FD-TD method of the dispersive characteristics associated with electronic polarization, Microw. Opt. Technol. Lett. **3**, 203 (1990).

[79] Rose M. Joseph, Susan C. Hagness, and Allen Taflove, Direct time integration of maxwell's equations in linear dispersive media with absorption for scattering and propagation of femtosecond electromagnetic pulses, Opt. Lett. **16**, 1412 (1991).

[80] Aaswath Raman and Shanhui Fan, Photonic Band Structure of Dispersive Metamaterials Formulated as a Hermitian Eigenvalue Problem, Phys. Rev. Lett. **104**, 087401 (2010).

[81] In cylindrical Mie theory, the incident field H_0 under transverse electric polarization is expanded by $\sum A_m J_m(kr)e^{im\theta}$. Quantities are scalar since both our geometry and excitation are objects on a 2D plane, with translational invariance in the perpendicular direction. The scattered field is $\sum B_m H_m^{(1)}(kr)$, while the interior field is $\sum C_m J_m(nkr)e^{im\theta}$. The Mie coefficients relate the scattered and interior fields to the incident field, $R_m = B_m/A_m$ and $T_m = C_m/A_m$. However, once the coefficients B_m are found, it is more accurate to calculate the total exterior electric field from the derivative of $H_0 + B_m H_m^{(1)}(kr)e^{im\theta}$ rather than from the expansion $\sum[A_m J_m(kr) + B_m H_m^{(1)}(kr)]e^{im\theta}$, thus partitioning the field into E_0 and the response of the structure, much like Eq. (26). For the interior fields, no such option is available to Mie theory, where $\sum C_m J_m(nkr)e^{im\theta}$ always represents the total field, including the portion attributable to H_0. This expansion is less accurate than Eq. (26), unless the truncation order m is very high. Thus, we limit the comparison to the exterior domain.